

Search for Dark Matter in Final State with Di-leptons and Missing Transverse Energy at CMS



By
Ijaz Ahmad
CIIT/SP21-RPH-019/ISB
MS Thesis
In
Physics

COMSATS University Islamabad,
Islamabad - Pakistan

Fall, 2022



COMSATS University Islamabad

Search for Dark Matter in Final State with Di-leptons and Missing Transverse Energy at CMS

A Thesis Presented to

COMSATS University Islamabad

In partial fulfillment

of the requirement for the degree of

MS Physics

By

Ijaz Ahmad

CIIT/SP21-RPH-019/ISB

Fall, 2022

Search for Dark Matter in Final State with Di-leptons and Missing Transverse Energy at CMS

A Post Graduate Thesis submitted to the Department of physics as partial Fulfillment of the requirement for the award of degree of M.S (Physics)

Name	Registration Number
Ijaz Ahmad	CIIT/SP21-RPH-019/ISB

Supervisor

Dr. Yasir Ali

Tenured Associate Professor

Department of Physics

COMSATS University Islamabad

January 2023

*This thesis is dedicated to my mother for her endless love, support,
and belief in me. Thank you for everything, Mom.*

Final Approval

This thesis titled

Search for Dark Matter in Final State with Di-leptons and Missing Transverse Energy at CMS

By

Ijaz Ahmad

CIIT/SP21-RPH-019/ISB

Has been approved

For the COMSATS University Islamabad

External Examiner:

Dr. Mansoor Ur Rehman

Associate Professor

Department of Physics

Quaid-e-Azam University Islamabad

Supervisor:

Dr. Yasir Ali

Tenured Associate professor

Department of Physics/CUI, Islamabad

Co-supervisor:

Dr. Ashfaq Ahmad

Director of EHEP

National Centre for Physics, Islamabad

HoD:

Dr. Waqas Masood

Professor

Department of Physics/CUI, Islamabad

Declaration

I Ijaz Ahmad (CIIT/SP21-RPH-019/ISB) hereby declare that I have produced the work presented in this thesis, during the scheduled period of study. I also declare that I have not taken any material from any source except referred to wherever due that amount of plagiarism is within acceptable range. If a Violation of HEC rules on research has occurred in this thesis, I shall be liable to punishable action under the plagiarism rules of the HEC.

Date: 24/01/2023

Signature of Student:

Ijaz Ahmad

CIIT/SP21-RPH-019/ISB

Certification

It is certified that the **Ijaz Ahmad (CIIT/SP21-RPH-019/ISB)** has carried out all work related to this thesis under my supervision at the department of physics COMSATS Institute of Information and Technology Islamabad and the work fulfill the requirement for award MS degree.

Date: 24/01/2023

Supervisor:

Dr. Yasir Ali
Tenured Associate Professor
Department of Physics
CUI, Islamabad

Head of Department:

Dr. Waqas Masood
Professor
Department of Physics
CUI, Islamabad

ACKNOWLEDGMENT

Firstly, all praise to Almighty Allah, who blessed me with the opportunity to complete my research work successfully.

I would like to express my sincere gratitude to my respected supervisor Dr Yasir Ali for his continuous support, motivation, and immense knowledge. It was a great privilege and honour to work under your supervision.

I am extremely thankful to Dr Ashfaq Ahmad who gave me a chance to work under his supervision at National Center For Physics Islamabad. This opened a door for me to participate in international conferences, seminars and schools and meet people all over the world. You always welcomed me whenever I faced a problem. Thank you so much for your support and always welcoming attitude. I had a wonderful and unforgettable time with you and learnt a lot.

I would especially like to thank Dr Muhammad Gul for your time, support, guidance and good will throughout this project. Without your support, I would not have been able to perform this interesting Dark Matter research project. I am thankful to Nouman, Atif and Umair for their support during the preparation and review of this document. I am grateful for the time I spent at NCP with Asif, Nouman, Zain, Saim, and Zahoor.

Lastly, I would like to thank my family for all their love and encouragement. My parents raised me with a love of science and supported me in all my endeavours. And most of all, for my loving, supportive, and encouraging, brother, Bait Ullah, and my sisters Farhat, Hafsa, and Shehla Gul whose faithful support during the whole process is highly appreciated. Thank you.

Ijaz Ahmad

Abstract

The Standard Model of particle physics does not predict the existence of Dark Matter, as indicated by many astrophysical observations. Dark Matter is predicted to be a matter of heavy particles called WIMPs (Weakly Interacting Massive Particles) by many theories beyond the Standard Model. In collider experiments, pair production can be used to search for WIMPs. There are many possible signatures but in this thesis, we have considered only two of them.

In the first section of the analysis, We have studied the production of a WIMPs pair with a Z boson decaying to a pair of leptons known as a mono-Z channel. The WIMPs leave the detector without interaction, resulting in events with a significant amount of missing transverse momentum and two highly-energetic opposite charge leptons. For this analysis, we have used simulated data for proton-proton collisions at 13 TeV using MadGraph5_aMC@NLO Monte-Carlo event generator. The Z boson and WIMPS are produced back to back at $\Delta\Phi = 3.14$. The results show that at $E_T^{miss} = 150$ GeV, the signal significance is high and the cut is applied at the transverse momentum of charge leptons at 150 GeV also discriminates the background. In the second part of the analysis, we have considered the production of a WIMPs pair associated with a Higgs boson decaying to a pair of bottom quarks known as a mono-Higgs channel. The absence of interaction between the WIMPs and the detector results in events with a significant amount of missing transverse momentum and two extremely energetic b-jets produced by the decay of the Higgs boson. For this part of the analysis we have used simulated data for proton-proton collisions at $\sqrt{s} = 13$ TeV, 13.6 TeV, 27 TeV and 100 TeV using MadGraph5_aMC@NLO Monte-Carlo Event generator. The results show that at the generator level, the signal is independent of the centre of mass energy. In both analyses, we have studied two parameters $\sin\theta$ (the mixing angle between the two neutral CP-odd Higgs bosons) and $\tan\beta$ (the ratio of the VEVs of the two CP even Higgs bosons).

Contents

1	Standard Model of Particle Physics	1
1.1	Historical Background	1
1.2	Fundamental Particles in Standard Model	2
1.2.1	Leptons	4
1.2.2	Bosons	5
1.3	Fundamental Interaction	6
1.4	Quantum Chromodynamics	11
1.4.1	Confinement	11
1.4.2	Asymptotic Freedom	11
1.5	Higgs	12
2	Dark Matter	14
2.1	Open questions of the SM	14
2.1.1	What is the Dark Matter	14
2.1.2	Gravity	14
2.1.3	Neutrino Masses	15
2.1.4	Matter anti-Matter Asymmetry	15
2.1.5	Three Generations of Matter	15
2.2	Evidence of Dark Matter	15
2.2.1	Galaxy Rotation Curve	15

CONTENTS

2.2.2	Gravitational lensing	17
2.3	Weakly Interacting Massive Particles (WIMPs)	18
2.4	Mono-X Collider Searches	18
2.5	Simplified Models	20
2.6	Signal Model	21
2.6.1	Two Higgs Doublet Model and 2HDM+a	21
3	The Large Hadron Collider and CMS Detector	25
3.1	Large Hadron Collider	25
3.1.1	The High Luminosity LHC Upgrade	26
3.2	Compact Muon Solenoid	27
3.2.1	CMS Detector Design	27
3.2.2	The CMS Coordinate Systems	29
3.3	The Tracking System	31
3.3.1	Silicon Pixel Detector	32
3.3.2	Silicon Strip Detector	33
3.4	The calorimetry sub-detectors	34
3.4.1	Electromagnetic Calorimeter	34
3.4.2	Hadronic Calorimeter	35
3.5	Solenoid Magnet and Iron Return Yoke	36
3.6	Muon Chamber	36
3.7	Trigger Concept	37
3.8	The CMS phse-2 Upgrade	37
3.8.1	Tracker Upgrade	38
3.8.2	Trigger Input	39
3.8.3	High Granularity Calorimeter	39
4	Simulation and Analysis Tools	42

CONTENTS

4.1	Events Generators	42
4.2	Event Generation at Parton Level	44
4.3	Parton showering and hadronisation	45
4.4	ROOT	46
5	The mono-Z($\ell\ell$)+E_T^{miss} Analysis	47
5.1	Signal samples	48
5.2	Standard Model Background Processes	49
5.2.1	$t\bar{t}$ production	49
5.2.2	Di-Bosons Processes	49
5.2.3	V+Jets	49
5.3	Variations of Parameter	49
5.3.1	Variation of $\text{Sin}\theta$	50
5.3.2	Variation of $\tan\beta$	51
5.3.3	Variation of m_χ	51
5.4	Missing Energy	52
5.4.1	Signal Significance	53
5.5	Transverse Momentum	54
5.6	Pseudorapidity of Signal and Background	56
5.7	ϕ of Signal and Background	57
5.8	delta Phi of $P_{T,Z}$ and P_T^{miss}	57
6	The mono-Higgs($b\bar{b}$)+E_T^{miss} Analysis	60
6.1	Signal samples	61
6.2	SM Background Processes	61
6.3	Variations of Parameter	62
6.3.1	Variation of $\sin\theta$	63
6.3.2	Variation of $\tan\beta$	63

CONTENTS

6.3.3	Variation of m_χ	64
6.4	Variation of Energy	65
7	Summary and Conclusions	67
	References	69

List of Figures

1.1	Properties of baryon[1]	3
1.2	QED interaction	7
1.3	The upper left diagram show Moller scattering, upper right diagram show Bhabba scattering and below diagram show Compton scattering.	8
1.4	The left diagram shows the interaction of quarks in QCD , middle and right diagram shows gluon gluon interaction [2].	9
1.5	Feynmann diagrams in weak interaction for w^- boson [3].	9
1.6	Feynmann diagrams in weak interaction for Z boson.	10
1.7	Semileptonic process for W^- mediator.	10
1.8	semileptonic process for Z mediator	10
1.9	Higgs's production mode cross section[4].	12
1.10	Higgs production modes[5].	13
1.11	Higgs decay modes[5].	13
2.1	Rotation curve of NGC 6503 galaxy.	16
2.2	An X-ray observation of the Bullet cluster obtained by Chandra X-ray Observatory. The red region represents the X-ray measurement of hot gas, while the blue area highlights the gravitational lensing image of total matter distribution. [6].	17
2.3	Pseudo Feynman diagram showing potential interaction between dark and SM sector. Taken from [7].	19

LIST OF FIGURES

2.4	These Feynman diagrams show DM production in association with an ISR gluon, photon, Z, W or a Higgs boson.	19
2.5	Feynman diagrams of $h+E_T^{miss}$ (top row) $Z+E_T^{miss}$ (second row) signals [8].	23
3.1	A schematic representation of LHC[9].	26
3.2	LHC project schedule including the plan for the upcoming high luminosity upgrade. Figure taken from [10].	28
3.3	A perspective view of the CMS detector [11].	29
3.4	The CMS detector transverse section with signatures of different types of detected[12]	30
3.5	The CMS coordinate system[13].	31
3.6	CMS tracker system[14].	32
3.7	Schematic diagram of the Silicon pixel Tracker[15].	33
3.8	Mechanical layout of the pixel and strip tracker[16].	33
3.9	The ECAL barrel and an ECAL endcap may be seen in a longitudinal image of a portion of the CMS electromagnetic calorimeter, with the preshower in the front. [17].	35
3.10	An overview of one-quarter of the CMS HCAL showing the four major components: the hadron barrel (HB), the hadron endcap (HE), the hadron outer (HO), and the hadron forward (HF) calorimeters.[18]. . . .	36
3.11	Drawing illustrating the various sub-detectors of the CMS experiment[19]	37
3.12	One fourth segment of the CMS Phase-2 tracker[20].	38
3.13	pT -trigger modules[21].	39
3.14	Cross section of CMS HGCAL. Figure 3.17 taken from[22].	40
3.15	FLUKA simulation of the particle fluence in $1\text{MeV}n_{eq}/\text{cm}^2$ accumulated in HGCAL after an integrated luminosity of $3000fb^{-1}$. The layout is shown in in r-z view. Figure 3.16 taken from [20].	41
4.1	Monte-Carlo simulations of LHC Collisions[23]	43

LIST OF FIGURES

5.1 A Feynman diagram shows the final state of the Z boson produced by the 2HDM+ a model, which decays into a pair of leptons and a pseudoscalar "a" which decay into pair of dark matter. (right) $b\bar{b}$ fusion, here h4 represent pseudoscalar a, (left) gg fusion	48
5.2 Feynman diagrams shows the background $t\bar{t}$ (top row left), ZZ (top row right), Z+jets (bottom row left), and W+jets (bottom row right)	50
5.3 E_T^{miss} distributions for mono-Z production for various values of $\sin\theta$. Other parameters are set to (2.6.3) using $M_a = 400$ GeV and $M_A=M_H=M_H^\pm = 700$ GeV.	51
5.4 The distribution shows that for $\tan\beta \leq 1$, we have maximum cross-section (left). E_T^{miss} distributions for mono-Z production (right). The 2HDM + a parameters are set to (2.6.3) using $M_a = 200$ GeV and $M_A=M_H=M_H^\pm = 700$ GeV.	52
5.5 E_T^{miss} distributions for mono-Z production. The distribution corresponds to different values of m_χ . Other parameters are set to(2.6.3) using $M_a = 300$ GeV and $M_A=M_H=M_H^\pm = 700$ GeV.	53
5.6 Significance of a signal.	54
5.7 Missing Transverse momentum distribution.	55
5.8 P_T distribution of Z boson.	56
5.9 Tranverse Momentum of charge leptons of ZZ and $t\bar{t}$ background.	56
5.10 Tranverse Momentum of signal and background.	57
5.11 η distribution of signal and background.	58
5.12 ϕ distribution of signal and background.	59
5.13 $\Delta\phi$ distribution of $P_{T,Z}$ and P_T^{miss}	59
6.1 The Feynman diagrams show the 2HDM+ a model processes where a heavy pseudoscalar A decay to Higgs and pseudoscalar a.	62
6.2 Feynman diagrams of Z+jets (left), W+jets(middle), and $t\bar{t}$ (right) background processes.	62

LIST OF FIGURES

6.3 E_T^{miss} distributions for mono-higgs. The distribution corresponds to various values of $\sin\theta$. The rest of the parameters are set to (2.6.3) using $M_a = 400$ GeV and $M_A = M_H = M_H^\pm = 700$ GeV.	63
6.4 E_T^{miss} distributions for mono-Higgs production in gg-fusion in the 2HDM + a model. The predictions shown correspond to pp collisions at 13 TeV. The 2HDM + a parameters are set to (2.6.3) using $M_H = M_A = M_H^\pm = 700$ GeV and $M_a = 200$ GeV.	64
6.5 E_T^{miss} distributions for mono-h production. The distribution corresponds to different values of m_χ . Other parameters are set to (2.6.3) using $M_a = 300$ GeV and $M_A = M_H = M_H^\pm = 700$ GeV.	65
6.6 E_T^{miss} distributions for mono-h production at 13, 13.6, 27, and 100 TeV. The presented results correspond to $\tan\beta = 1$. Other parameters are set to (2.6.3) using $M_a = 200$ GeV and $M_A = M_H = M_H^\pm = 700$ GeV.	66

List of Tables

1.1	Properties of quarks[1]	3
1.2	Properties of meson	4
1.3	Properties of leptons[24]	5
1.4	Properties of boson [25]	6
1.5	Four Fundamental Forces of nature[1].	6
2.1	Parameters description of 2HDM+a [17].	24
3.1	The essential real parameters for the LHC are mentioned in the Table. .	27
5.1	The SM background in the signal region.	53
5.2	Applied energy cuts on the signal.	54

CHAPTER 1

Standard Model of Particle Physics

1.1 Historical Background

The definition of fundamental particles changes with the passage of time. In about 400 B.C, the Greek philosophers believed that matter is made up of atoms, however, we know that the atom is not a fundamental particle thus the passage of time as technology evolves and the discovery of new particles results in the development of elementary particle physics.

The elementary particle physics journey starts when the electron was discovered by J.J Thomson in 1897 [26]. Thomson discovered electrons in the cathode ray tube, he demonstrate that some rays emerging from the cathode in the cathode ray tube can be deflected by the magnet suggesting that these rays have some charge. Later he measured the charge and mass of the electron. In 1911, Rutherford and his co-workers while performing their experiment on the Gold foil discovered that there exists a small dense matter inside the atom from which some of the alpha rays have deflected at various angles, he called it nucleus [27] and demonstrated that electrons revolve around the nucleus in circular orbits like the planetary system as shown in figure 1.1. Later in 1919, he also discovered proton [27]. In 1932, another scientist James Chadwick discovered an electrically neutral particle called a neutron which has almost the same mass as that of a proton [28]. This was considered almost the final recipe for the structure of an atom. The Standard Model of Particle Physics describes the fundamental particles of matter

and how they interact, namely electromagnetic, weak, and strong forces, but not gravity. In 1957, Chien-Shiung Wu demonstrated that weak interactions have no parity conservation [29]. In 1961, Sheldon Glashow and Abdus Salam unified the electromagnetic and weak interactions. [30]. Martin Perl discovered the tau in the mid of 1970s at the Stanford Linear Accelerator Center in California [31]. The Z boson is a neutral weak gauge boson discovered by physicists at CERN's Super Proton Synchrotron in 1983 [32]. At the Fermi Lab in April 1995, top quark was discovered. At the LHC, the mass of Higgs 125.35 GeV was found in 2012 [33].

1.2 Fundamental Particles in Standard Model

A particle can be classified as either a Boson or a Fermion. Fermions are those particles which obey the Pauli exclusion principle. Their spin is a half-integer. The following two groups of fermions are:

Quarks

Quarks and antiquarks have colour charges, so that's why they participate in strong interaction. They have $1/2$ integer spin. Three generations of quarks exist according to the standard model. Up (u) and down (d) quarks are of the first generation. The charm (c) and strange (s) quarks are of the second generation. The strangeness is not conserved in the weak interaction. The top (t) and the bottom (b) are of the third generation. Top, up, and charm Quark have a charge of $(2/3)e$ and antiparticles have an opposite charge. bottom, down and strange Quark has a charge of $(-1/3)e$ and antiparticles have an opposite charge. Table 1.1 summarises the key properties of six quarks.

Quarks are always combined in such a way that they have no color charge, which is known as Hadron. Hadrons are further divided into two types: baryons and mesons.

Baryon

Those particles, which are made up of three quarks, are called Baryon. Examples are the proton, neutron and lambda etc. which are made of uud, udd, and uds quarks respectively. Baryon number conservation is the basic law for the reaction to be allowed.

Table 1.1: Properties of quarks[1]

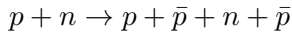
Quarks	Baryon number	Strangeness
u	$\frac{1}{3}$	0
d	$\frac{1}{3}$	0
c	$\frac{1}{3}$	0
s	$\frac{1}{3}$	-1
t	$\frac{1}{3}$	0
b	$\frac{1}{3}$	0

Baryon number can be calculated as:

$$B = 1/3(n_q - \bar{n}_q)$$

where n_q is no of quarks and \bar{n}_q is anti no of quarks.

An example of a baryon number reaction is:



Baryon numbers:

Before: $1 + 1 = 2$

After: $1 + 1 + 1 - 1 = 2$

Therefore, the above reaction is allowed because of the conservation of the baryonic number. Figure 1.1 summarize the key properties of baryon.

qqq	Q	S	Baryon
<i>uuu</i>	2	0	Δ^{++}
<i>uud</i>	1	0	Δ^+
<i>udd</i>	0	0	Δ^0
<i>ddd</i>	-1	0	Δ^-
<i>uus</i>	1	-1	Σ^{*+}
<i>uds</i>	0	-1	Σ^{*0}
<i>dds</i>	-1	-1	Σ^{*-}
<i>uss</i>	0	-2	Ξ^{*0}
<i>dss</i>	-1	-2	Ξ^{*-}
<i>sss</i>	-1	-3	Ω^-

Figure 1.1: Properties of baryon[1]

Meson

Those particles, which are made of one quark and antiquark pair ($q\bar{q}$), is called Meson. Meson has zero net colour as well as zero baryon number. "Pseudoscalar mesons" are mesons that have no spin. "Vector mesons" are mesons that have one spin. All mesons with $l = 0$ have odd parity. Examples are pion, phi and rho etc. Some information about mesons is given in table 1.2.

Table 1.2: Properties of meson

Mesons	Mass (MeV)	J^{PC}	I
π^-, π^0, π^+	138.0	0^{-+}	1
η	547.3	0^{-+}	0
ω	781.9	1^{--}	0
ϕ	1019.5	1^{--}	0

1.2.1 Leptons

Leptons and anti-leptons have no colour charge, that is the reason they do not participate in the strong interaction. These are spin 1/2 particles and come in three generations. The electron and its neutrino are included in the first generation. The muon and its neutrino are included in the second generation. The tau and its neutrino are included in the third generation. Tau, Muon, and Electron neutrinos are chargeless but have a very small mass due to neutrino oscillation. By the Donut collaboration in 2000, the tau neutrino was discovered. All neutrinos are left-handed neutrinos and contrast for its anti-particles. Their opposite lepton number signs and helicity distinguish them from neutrinos. Leptons participate in electromagnetic, weak, and gravitational interactions. The leptonic numbers are $L_e = 1$, $L_\mu = 1$ and $L_\tau = 1$.

The lepton number conservation is the basic law for the reaction to be allowed. One example of muon decay in terms of lepton number is:

$$\mu \rightarrow e^- + e^+$$

$$L_e: 0 \rightarrow 1 + 0 - 1$$

$$L_\mu: 1 \rightarrow 0 + 1 + 0$$

Therefore, the above reaction is allowed because of the conservation of leptonic number.

Table 1.3 summarises the key properties of Lepton and antilepton.

Table 1.3: Properties of leptons[24]

Name	Symbol	Antiparticle	Charge	Mass (Mev)
Electron	e^-	e^+	-1	0.511
Electron neutrino	ν_e	$\bar{\nu}_e$	0	small, but non-zero
Muon	μ^-	μ^+	-1	105.7
Muon neutrino	ν_μ	$\bar{\nu}_\mu$	0	<0.19
Tau	τ^-	τ^+	-1	1776
Tau neutrino	ν_T	$\bar{\nu}_T$	0	< 18.2

1.2.2 Bosons

The fundamental forces like as the electromagnetic, strong, and weak forces are mediated by the gauge bosons, which are force carriers.

Bosons are particles with integer spin and obey the Bose-Enstein statistics. Bosons are further divided into the Guage and Scalar Boson classes.

Guage Boson

Guage bosons have spin 1. There are three types of mediators included, which are as follows:

1. The mediator of the electromagnetic interaction is called a photon and its symbol is γ .
2. The mediator of the weak interaction is called intermediate vector boson and their symbols are W and Z.
3. The strong interaction mediator is called a gluon its symbol is g.

Scalar Bosons

Scalar bosons are a type of subatomic particles that are associated with a type of force known as a scalar field. These particles are characterized by a spin of zero and are their

own antiparticles. In the Standard Model, the Higgs boson is a scalar boson with a mass of 125 GeV.

Table 1.4: Properties of boson [25]

Gauge boson	spin	Charge	Mass	Force
Photon γ	1	0	0	electromagnetic
W-boson W^+, w^-	1	± 1	80.4 Gev	weak
Z-boson Z^0	1	0	91.2 Gev	weak
gluons g	1	0	0	strong
graviton G	2	0	0	Gravitational

1.3 Fundamental Interaction

The four fundamental forces in Nature are electromagnetic, weak, strong and gravitational force. The strength of strong, electromagnetic, weak and gravitational interactions are 10 , 10^{-2} , 10^{-13} , and 10^{-42} , respectively. Table 1.4 summarises the key properties of four fundamental forces.

Table 1.5: Four Fundamental Forces of nature[1].

Force	Strength	Theory	Mediator
Strong	10	Chromodynamics	Gluon (g)
Electromagnetic	10^{-2}	Electrodynamics	Photon (γ)
Weak	10^{-13}	Flavordynamics	W^+, W^- and Z^0
Gravitational	10^{-42}	Geometrodynamics	Gravitons (G)

Geometrodynamics is the physics theory that describes space time gravitational force and gravitational force in terms of geometry. A graviton is a mediator of gravitational force. Mostly people think that the gravity is too much weak to demonstrate its role in

the elementary particle physics.

The electromagnetic interactions are described by the theory of QED. In QED, the photon acts as a mediator.

In figure 1.2, when an electron enters through electromagnetic interaction, it emits or

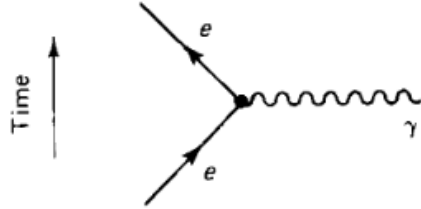


Figure 1.2: QED interaction

absorbs the photon and then leaves.

The upper left diagram in figure 1.3 shows the Coulomb repulsion of two electrons mediated by the photon exchange. This process is called Moller scattering.

$$e^- + e^- \rightarrow e^- + e^-$$

The upper right diagram in figure 1.4 shows the Coulomb attraction of electrons and positrons mediated by the exchange of photons. This process is called Bhabha scattering.

$$e^+ + e^- \rightarrow e^- + e^+$$

In Figure 1.4 below, the diagram shows the Compton scattering, which is the scattering of a photon with an electron by losing some parts of its energy.

$$e^- + \gamma \rightarrow \gamma + e^-$$

The physical theory that describes strong interaction is called Quantum chromodynamics. The mediator between two quarks in a strong interaction is called a gluon. Gluon carries bicolour, i.e colour and anti-colour. The colour of the quark may vary during the process $q \rightarrow q + g$. A blue up-quark, for example, could become a red up-quark by conversion. The gluon must carry away the difference in this case, one unit of blueness and minus one unit of redness—because colour (like charge) is always conserved as seen in Figure 1.4 (left).

"Red" (r), "blue" (b), and "green" (g) are the three colours of quarks. There are $3 \times 3 = 9$ possibilities here, but there are 8 different types of gluons exist because the linear combi-

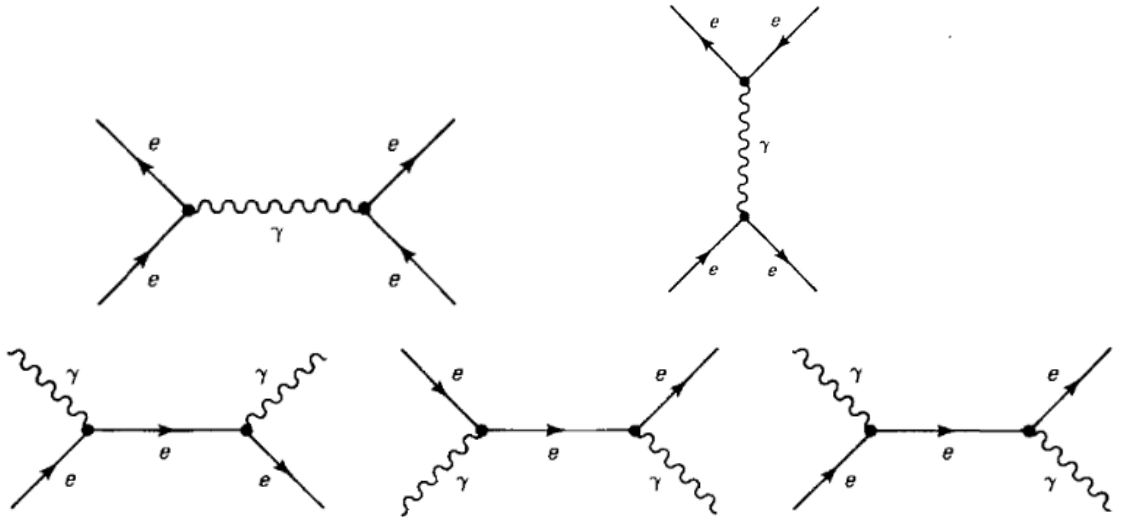


Figure 1.3: The upper left diagram show Moller scattering, upper right diagram show Bhabha scattering and below diagram show Compton scattering.

nation of red+green+blue is a neutral particle which is physically not allowed because the gluon should be color particle.. Since gluons carry color, unlike photons, that's the reason they directly couple with other gluons. The middle and right side diagram of figure 1.5 shows gluon gluon interaction:

The critical parameter turns out to be:

$$a = 2f - 11n$$

where f is number of flavour and n is colour.

If the value of a is positive, then the effective coupling in QED increases at short distances and contrasts for negative values. In the Standard Model, $f= 6$ and $n= 3$, so $a= -21$. The origin of asymptotic freedom is due to decreasing QCD coupling at a short distance.

The physical theory that describes weak nuclear interaction is called Flavourdynamics. CP, Parity and Strangeness are not conserved in weak interaction. Weak interactions are divided into two types: charge-mediated by W's and neutral-mediated by Z bosons. All quarks and leptons participate in weak interactions.

The left side of the Feynman diagram in figure 1.5 shows a negative lepton is converted into a corresponding neutrino by emitting w^+ boson.

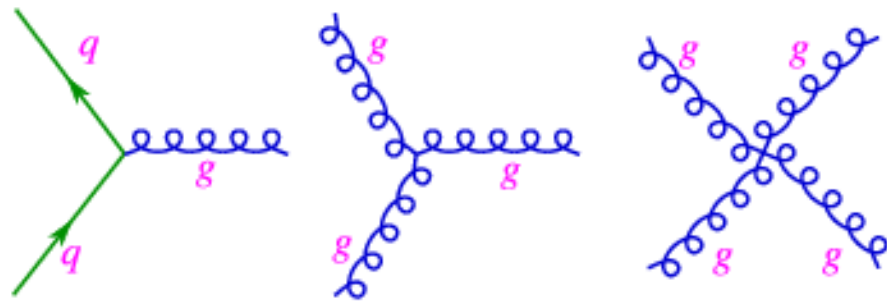


Figure 1.4: The left diagram shows the interaction of quarks in QCD , middle and right diagram shows gluon gluon interaction [2].

$$l^- \rightarrow w^+ + \nu_l$$

The right side Feynman diagram in figure 1.5 is shown for $e^- + \nu_e \rightarrow e^- + \nu_e$

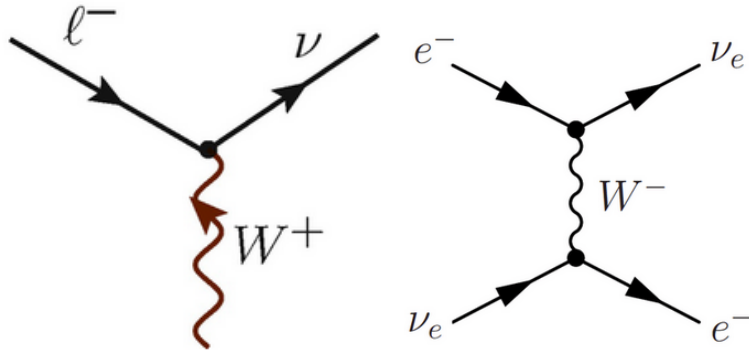


Figure 1.5: Feynmann diagrams in weak interaction for w^- boson [3].

Left side diagram in figure 1.6 shows a lepton can be converted into another lepton by the emission of a Z boson.

$$l \rightarrow l + Z$$

The right side diagram in figure 1.6 for the process of:

$$(\nu_\mu + e \rightarrow \nu_\mu + e)$$

Quarks can also interact in weak interactions. The fundamental charged vertex's Feynmann diagram is as follows:

In Figure 1.7, the emission of a W^- boson transforms a $-1/3$ charge quark into a $+2/3$

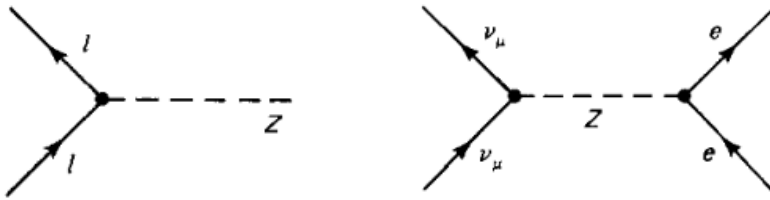


Figure 1.6: Feynmann diagrams in weak interaction for Z boson.

charge quark. The Feynman diagram for the semileptonic process ($d + ve \rightarrow u + e$):

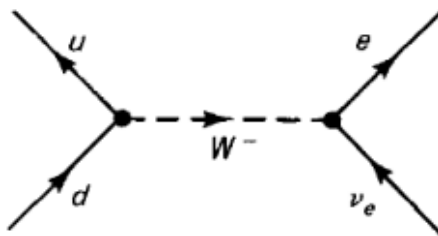


Figure 1.7: Semileptonic process for W^- mediator.

The Feynmann diagram for the process ($V_\mu + p \rightarrow V_\mu + p$):

as shown in Figure 1.8.

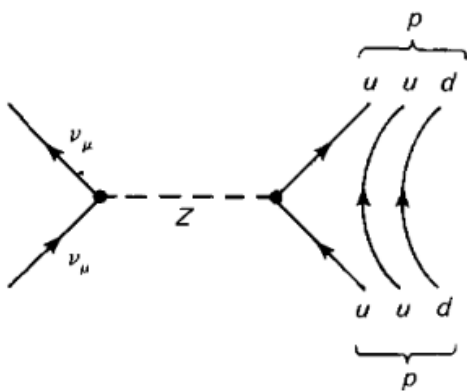


Figure 1.8: semileptonic process for Z mediator

1.4 Quantum Chromodynamics

Quarks and gluons have strong interactions with one another, and partonic interactions inside hadrons are explained by the quantum field theory known as QCD. In QED, only positive and negative charge exist but in QCD we have color charge (red, green, and blue). These colors have nothing with light color.

A QCD force carrier called a gluon has a nonzero color quantum number, and as a result, it can form interaction vertices with three or four gluons. In QCD, gluons interact with themselves in a way that differs greatly from the (Abelian) quantum field theory Quantum Electrodynamics (QED), which does not allow photons to interact with themselves since they do not possess electric charges. Quarks and gluons are collectively called 'partons' when they are contained within hadrons. QCD is characterized by color confinement and asymptotic freedom.

1.4.1 Confinement

In quantum chromodynamics (QCD), confinement refers to the phenomenon in which the strong nuclear force between quarks and gluons is able to confine them within hadrons (such as protons and neutrons). This means that quarks and gluons are not observed as individual particles, but rather are always found bound together inside hadrons. The mechanism behind confinement in QCD is not fully understood, but it is an important and fundamental property of the strong force that plays a key role in shaping the behavior of matter at the subatomic scale.

1.4.2 Asymptotic Freedom

Asymptotic freedom is a property of the strong nuclear force (described by the theory of quantum chromodynamics, or QCD) that allows quarks and gluons to behave as if they are almost free particles at very high energies or short distances. This behaviour is in contrast to the strong force at lower energies, where quarks and gluons are confined within hadrons and do not interact directly with each other. During the 1970s, David Gross, Frank Wilczek, and David Politzer proposed the concept of asymptotic freedom, which was then confirmed by experiments conducted in the 1980s. It is an important feature of QCD that helps to explain the behaviour of matter at high energies, such as

those found inside particle accelerators.

1.5 Higgs

The theoretical framework of the SM can calculate the branching ratios of the Higgs bosons. Details are given regarding the SM Higgs boson.

Production Modes

The biggest Higgs boson production rate at the LHC at $\sqrt{s} = 13\text{TeV}$ (44pb) is gluon-gluon fusion(ggF). The virtual top quark is a mediator in ggF. Higgs boson production channel at the LHC, Vector Boson fusion(VBF) has the 2nd highest production cross-section (3.7pb). Other production methods include associated production with weak vector bosons V-H, which has a production cross-section of 2.2 pb at 13 TeV, as well as associated production with top quarks ttbar-H, which has a production cross-section of 0.51 pb at 13 TeV.

	process	8 TeV	13 TeV
ggF	gluon-gluon fusion	19 pb	44 pb
VBF	vector-boson fusion	1.6 pb	3.7 pb
VH	associated production	1.1 pb	2.2 pb
ttH	associated production	0.13 pb	0.51 pb

Figure 1.9: Higgs's production mode cross section[4].

The Feynmann diagrams for Higgs boson are:

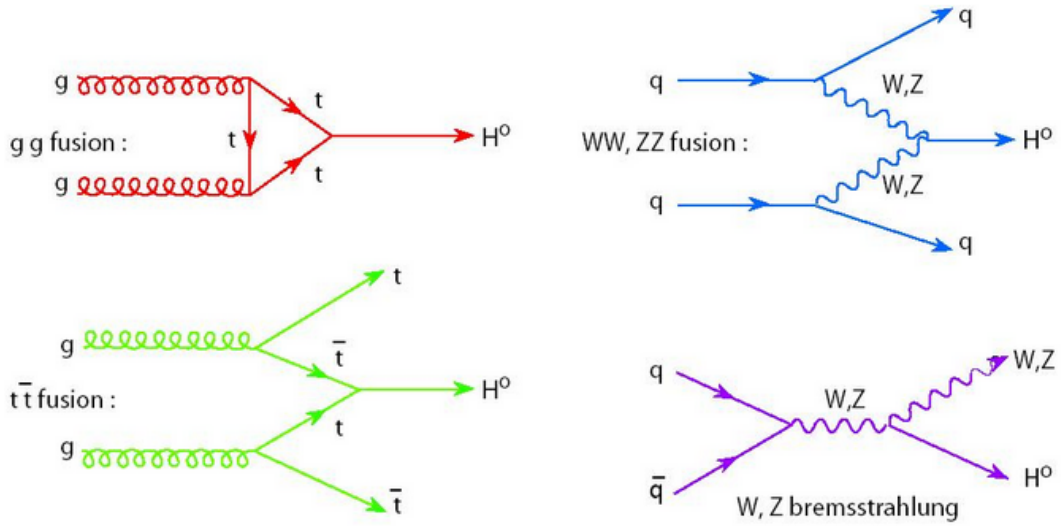


Figure 1.10: Higgs production modes[5].

Decay Modes

Because of its low stability, the Higgs boson can only be identified in decay modes. The heavy bottom quark b has a high Yukawa coupling to the Higgs boson, the leading decay mode of the Higgs boson is $H \rightarrow bb$. The decay into two vector bosons $H \rightarrow VV$ with $V = W, Z$ is another common decay mechanism. Another important Higgs boson decay channel is $H \rightarrow \gamma Z$ via virtual W boson loops. The below figure summarises Higgs boson's decay modes.

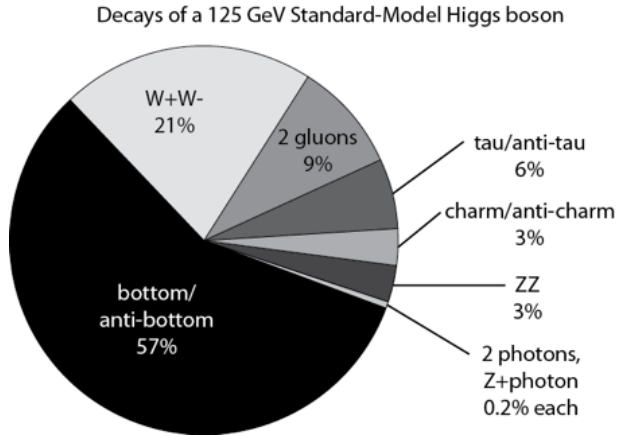


Figure 1.11: Higgs decay modes[5].

CHAPTER 2

Dark Matter

2.1 Open questions of the SM

Despite being a successful theory, the SM is viewed as being lacking in some key areas. Some of the unanswered questions that the SM leaves are covered below:

2.1.1 What is the Dark Matter

Cosmological observations indicate that an important fraction of the mass of the Universe is unseen “Dark Matter” and what we see from galaxies and stars represents 4.8 % of the Universe [34, 35]The SM does not offer any candidate for dark matter. An extension of the SM theory is needed to explain the existence of dark matter. Detailed studies of the dark matter search are presented in this thesis.

2.1.2 Gravity

Among the four fundamental interactions, gravity is the weakest and is responsible for the macroscopic structure of the Universe. The SM describes the strong and electroweak forces, but it doesn’t provide any information about gravity because it is based on the principle of quantum mechanics, which is a theory that describes the behaviour of very small particles, while gravity is a long-range force that operates on a much larger scale. A complete theory attempts to unify the four fundamental forces into one but it has not been possible yet.

2.1.3 Neutrino Masses

Neutrinos in the SM are massless particles. However, experiments showed that neutrinos created with specific flavor can be measured with a different flavor. This neutrino oscillation phenomenon between different flavors can't happen if neutrinos are massless [36–38].

2.1.4 Matter anti-Matter Asymmetry

Why there is no antimatter in the universe? The early stages of the universe need to be understood, either more matter was created or an equivalent amount of matter and antimatter were created, but somehow antimatter vanished. In the SM, there is no mechanism to explain the dominance of matter over antimatter.

2.1.5 Three Generations of Matter

Why there are three generations of quarks and leptons, as well as why fermion masses vary by many orders of magnitude, is not explained by the Standard Model.

2.2 Evidence of Dark Matter

According to cosmology, the universe's total mass-energy is made up of roughly 4.8 % conventional matter, 25.8 % dark matter (DM), and 69.4 % dark energy, meaning that the vast bulk of our universe is invisible. [34, 35]. DM has not been directly observed, but some of the cosmic observational evidence given below allows us to estimate its existence and properties. Those observations don't provide information about the DM nature, but they provide constraints on its properties.

2.2.1 Galaxy Rotation Curve

The first indication of DM existence was introduced by Fritz Zwicky [39] in 1933 when calculating the mass of the Coma Cluster using the virial theorem that relates the kinetic energy of the system to its potential energy. He indicates that the calculated galaxy mass is around two orders of magnitude larger than what is expected from the visible matter which implies the existence of non-luminous (dark) matter. The idea of dark

matter was accepted later by scientists after the studies of galaxy rotational curves. The rotational curve describes the velocity of the visible stars or gas in the galaxy versus their radial distance from that galaxy's center. According to Newtonian dynamics, it is expected that the velocity $v(r)$ of the visible matter decreases as $1/r$, following equation 2.2.1, while moving from the center of the galaxy where most of the luminous matter is located as shown in Figure 2.1 (left) by the red curve

$$v(r) = \sqrt{\frac{GM(r)}{r}} \quad (2.2.1)$$

where G is Newton's constant and $M(r)$ is the mass of the visible matter of the galaxy at a radius r . But Ford and Rubin found that the rotational velocity remains constant while moving from the centre of the galaxy as shown in Figure 2.1 (left) by a white curve [40]. This observation leads to the idea of the presence of a non-luminous dark matter halo in the galaxy. As shown in Figure 2.1 (right), the rotational curve of the NGC 6503 galaxy describes the observed rotation velocity compared to the expected rotation velocity assuming a spherical halo of dark matter and no coupling between dark matter and visible matter. According to data and expectations, the galaxy centre is mainly made up of visible matter, whereas the dark matter halo dominates the galaxy at large radii. [40].

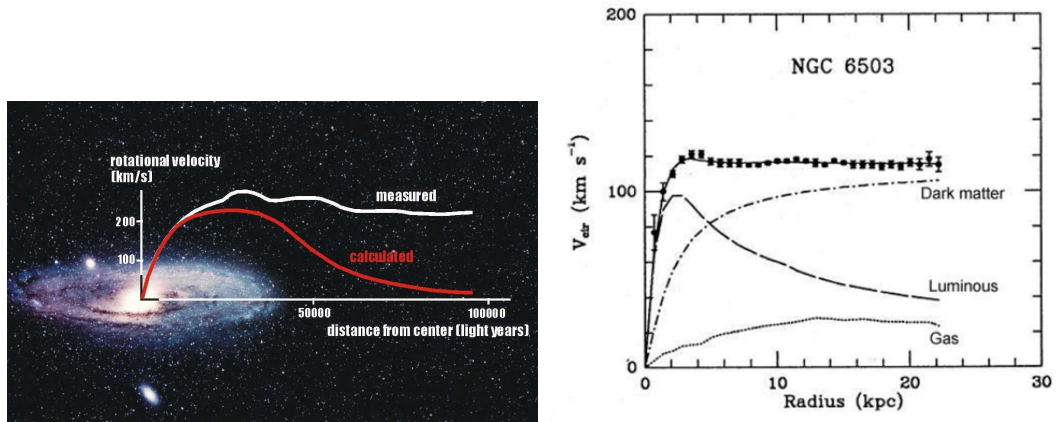


Figure 2.1: Rotation curve of NGC 6503 galaxy.

2.2.2 Gravitational lensing

A simple definition of gravitational lensing is “mass bends light”. When light from a distant object passes close to a big object (and hence through its gravitational field), the light will bend, causing the picture of the object to be distorted. Massive objects with strong gravitational fields include galaxies and clusters of galaxies [41, 42]. The bent light will refocus somewhere else producing single or multiple images of the light source, arcs, or even Einstein rings. The bending of the light depends on the mass of the object, the more massive the object means a stronger gravitational field, more bending of the light and hence more distortion of the image. It is possible to estimate the object’s mass from the intensity of the image distortion. The image in figure 2.2 shows a lensed and X-ray image of galaxy cluster 1E 0657-56. During the collision of two galaxies, the gas particles (the “normal” matter) will interact electromagnetically with each other and slow down. On the contrary, dark matter interacts only through gravity without undergoing electromagnetic interaction. So the majority of the light is coming from the hot gas. The pink region in the image shows X-ray emitting gas, while the blue region shows dark matter located indirectly through gravitational lensing within the cluster. The observations show that most of the visible matter is now in the centre of the image, but the lensing tells us that most of the mass lies further out which indicates the presence of dark matter.



Figure 2.2: An X-ray observation of the Bullet cluster obtained by Chandra X-ray Observatory. The red region represents the X-ray measurement of hot gas, while the blue area highlights the gravitational lensing image of total matter distribution. [6].

2.3 Weakly Interacting Massive Particles (WIMPs)

As discussed in the previous section It is worth noting that there is strong experimental evidence in favor of DM. These experiments, however, are unable to resolve the question of what constitutes the particle nature of DM. Among the fascinating hypothetical particle categories that have gained considerable attention WIMPs, denoted by χ . It is not precisely defined what would constitute a WIMP, but observation sets certain constraints. WIMPs are generally defined as new fundamental particles beyond the Standard Model whose masses fall in the range of 1 to 10^5 GeV, with gravitational interaction as the only interaction, or possibly a weak interaction that is weaker or as weak as the weak interaction. The lifetime of a WIMP needs to be comparable to the age of our universe to explain structure formations and clustering of matter. Furthermore, the particle needs to be non-relativistic, also known as "cold", in order to explain the structure formations and clustering of matter. DM's observed abundance could be explained by particles exhibiting these characteristics, provided they went through a "thermal freeze-out" process. If the early Universe's temperature was high enough to maintain WIMPs in thermal equilibrium with the Standard Model particles, this would have resulted in the formation and annihilation of WIMP pairs.

$$\chi\chi \leftrightarrow SM$$

2.4 Mono-X Collider Searches

It might be able to create DM in a lab setting and investigate its properties if DM particles interact with SM particles. This would suggest that the mediator connecting the SM and dark sectors has been produced. Three methods of DM detection are illustrated using the pseudo-Feynman diagram in Figure 2.3. The interaction in the diagram is not explicitly shown and is dependent on the particular model proposed.

If the diagram's time axis were to be treated from left to right, it would imply that DM would annihilate into SM particles. One can suppose that this process occurs in regions of the universe where DM is most dense. This type of search is primarily performed by astrophysical experiments, and it is called an "indirect search". By flipping the diagram and treating the time axis as vertical, we would see scattering.

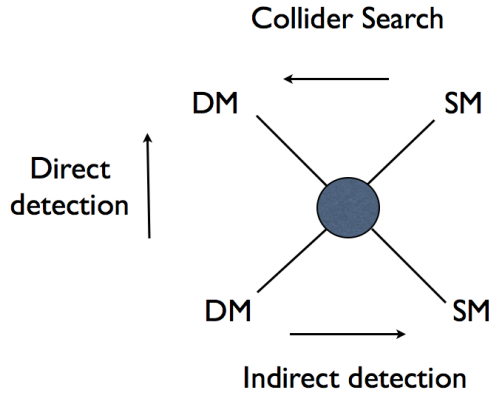


Figure 2.3: Pseudo Feynman diagram showing potential interaction between dark and SM sector. Taken from [7].

The DM scatters SM particles similarly to how neutrinos scatter atomic nuclei. This type of search is known as "direct search". The issue with both direct and indirect searches is that they rely on cosmic data, which introduces a number of astrophysical uncertainties. The diagram shows SM annihilation into DM particles when the time axis is read from right to left. This technique is known as a "collider search" because it is most likely to take place at particle colliders. . Collider searches offer the opportunity to examine DM in a controlled environment, in contrast to indirect and direct searches. Additionally, colliders are particularly sensitive to low DM masses of a few GeV, a range that is currently unreachable with direct detection methods.

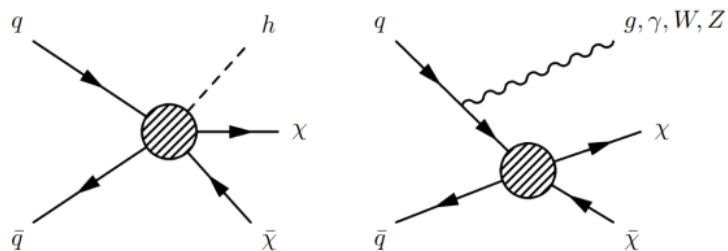


Figure 2.4: These Feynman diagrams show DM production in association with an ISR gluon, photon, Z, W or a Higgs boson.

Figure 2.3 demonstrates qualitatively how DM might be produced, but it does not provide information on how it might be detected in collider experiments. Particle detectors

depend on the electromagnetic interactions of charged particles, rendering DM invisible to such a device. However, if DM is produced together with an SM particle. The imbalance in total transverse momentum, also known as missing transverse energy, can be used to determine the presence of DM particles. In the LHC, ISR (initial state radiation) is a process whereby initial state particles emit particles like hard gluons, photons and radiate the heavier Higgs boson or massive gauge boson. Feynman diagrams for such processes as seen in Figure 2.4. The DM particle pair is produced along with the standard model particles like jets, Higgs bosons or vector gauge bosons and this process is known as mono-X searches. There have been many mono-X searches done at the LHC, and a review from 2018 is available here [43]. However, mono-Z mono-Higgs will be the main topic of this thesis. It should be noted that despite the possibility that the same ISR mechanism may produce a mono-Higgs signal, this possibility is heavily suppressed by the Yukawa coupling of the Higgs to lighter quarks. To build a model that predicts mono-h and mono-Z signatures, will serve as theoretical foundation of this thesis, it is required to extend the Higgs sector, as we will see in section 2.6.

2.5 Simplified Models

The so-called simplified model is an alternate strategy to effective field theory (EFTs). With additional degrees of freedom and at least one mediating particle, these models extend the contact interaction from EFT. Theoretical control can be increased beyond what is possible with EFT by adding more parameters to the theory. Simplified models are created to have as few parameters as possible, but to still be complete enough to properly represent essential physics at the energies explored by colliders. The more thorough theory, which integrates out all but the lightest degrees of freedom in the dark sector, can be seen as the limit of the simplified model. The resulting model usually has one stable DM candidate and at least one mediator, and is usually represented by a tree diagram Feynman diagram. A summary of the dark matter simplified models utilised in the initial LHC Run-2 searches is available here [44]. However, for the sake of this thesis, the group of models that will be examined will be those in which the mediator sector consists of an extended Higgs sector plus a further spin-0 particle.

2.6 Signal Model

The SM theory has various extensions that offer dark matter candidates and novel SM-DM interactions. The simplest extensions are the simplified models of DM production. Those models follow the following requirements [45]:

- The DM particle should be stable or lives long enough to escape the LHC detectors.
- The model should contain a mediator that couples the SM - DM sectors.
- The model should fulfil Lorentz invariance.
- The additional interaction terms between the SM and DM sector shouldn't violate the SM symmetries. This means that the baryon and lepton numbers should be conserved.

2.6.1 Two Higgs Doublet Model and 2HDM+a

As in section 1.3 the open questions that SM is not able to explain need the presence of new physics. The simplest possible extension of the SM is the two Higgs doublet model (2HDM) [46]. The 2HDM is generated by adding another new doublet to the complex scalar doublet of the SM. There are different types of 2HDM theories depending on which type of fermions couples to which doublet. In the type-II 2HDM, one of the doublet Φ_u couples to the up type quarks only while another doublet Φ_d couples to leptons and the down quarks.

$$\mathcal{L} \supset -y_u Q \bar{\Phi}_u u y_d Q \bar{\Phi}_d d \bar{d} + y_l L \Phi_d \bar{l} + h.c \quad (2.6.1)$$

where y_u , y_d , and y_l , represent the yukawa couplings of the Higgs doublets with the fermions and leptons. After the symmetry breaking, the new doublets acquire the VEVs v_u and v_u leading to the following parametrization: where h , H are the neutral CP-even

$$\begin{aligned} \Phi_d &= \frac{1}{\sqrt{2}} \begin{pmatrix} -\sin(\beta) H^+ \\ \nu_d - \sin(\alpha)h + \cos(\alpha)H - i \sin(\beta)A^0 \end{pmatrix} \\ \Phi_u &= \frac{1}{\sqrt{2}} \begin{pmatrix} \cos(\beta) H^+ \\ \nu_u + \cos(\alpha)h + \sin(\alpha)H + i \cos(\beta)A^0 \end{pmatrix} \end{aligned}$$

scalars with masses m_h and m_H respectively, H^\pm is the heavy charged scalar with mass m_{H^+} and its antiparticle H^- with mass m_{H^-} , A^0 is neutral CP odd with mass m_{A^0} . The

angle β represents ratio of the Vacuum Expectation Values of the two CP even Higgs bosons $\tan\beta = \frac{\nu_u}{\nu_d}$ and α is the mixing angle between the CP even scalars h and H . The scalar h is considered as SM Higgs boson with mass $m_h = 125 GeV/C^2$.

In the 2HDM with pseudoscalar mediator “denoted 2HDM+a” the interaction between the SM and DM particles are governed by the CP-odd spin-0 mediator [47, 48]. This is done by mixing the pseudoscalar P with CP-odd scalar from the Higgs doublet:

$$L \supset P(ib_p \phi_u^+ \phi_d + h.c) + P^2(\lambda_{p1} \phi_u^+ \phi_u + \lambda_{p2} \phi_d^+ \phi_d) \quad (2.6.2)$$

where b_p , λ_{p1} and λ_{p2} are the trilinear and quartic portal couplings.

The portal coupling b_p mixes the two neutral CP-odd weak eigenstates (A , a) with angle β representing the associated mixing angle. Here “ a ” is the extra degree of freedom not present in the 2HDM. The heavy pseudoscalar A^0 couples to the SM and the dark sector, the light pseudoscalar a couples directly to DM particles. In total we have six physical Higgs bosons: a light neutral CP-even scalar h , assumed to be the observed 125 GeV Higgs boson; a heavy neutral CP-even scalar H ; a neutral CP-odd scalar A^0 ; a light CP-odd scalar a ; and two charged scalars H^\pm .

In this search different model parameters have been scanned over while other parameters are fixed. The following parameters have been scanned:

- $\tan\beta$ is the ratio of the vacuum expectation values of the light and heavy scalar h and H .
- The angle $\sin\theta$ associated with the mixing between the light and heavy pseudoscalar a and A .
- The Dark matter mass m_χ .

we used the following benchmark parameters in this research[49]

$$M_H = M_A = M_H^\pm, m_\chi = 10 \text{ GeV}$$

$$\cos(\beta - \alpha) = 0, \tan\beta = 1, \sin\theta = 0.35,$$

$$y_x=1, \quad \lambda_1 = \lambda_{P1} = \lambda_{P2} = 3 \quad (2.6.3)$$

There are numerous mono-X signatures that result from the 2HDM+a model. One such signature occurs when an SM particle X and the mediator 'a' are produced resonantly. Then 'a' decays into a DM pair ($a \rightarrow \chi\bar{\chi}$) produced the mono-X signal. . There are several mono-X channels that allow studying DM pair production, but we have studied only $h+E_T^{miss}$, $Z+E_T^{miss}$. The Feynman diagrams for the above mono-X channels as seen in Figure 2.5.

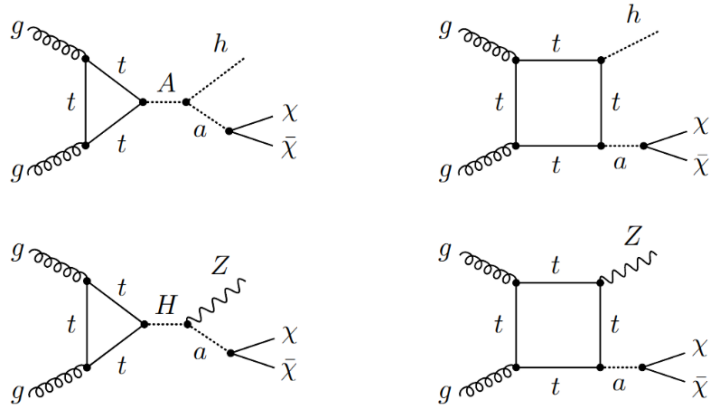


Figure 2.5: Feynman diagrams of $h+E_T^{miss}$ (top row) $Z+E_T^{miss}$ (second row) signals [8].

From top left diagram in Figure 2.5, one can see that it is possible to produce the pseudoscalar A if $M_A > m_a + m_h$. As a result, resonant mono-Higgs production will dominate the top-right diagram. Similarly for the mono-Z channels, if the $M_H > m_a + m_Z$ (bottom left diagram). As a result, resonant mono-Z production will dominate the bottom-right diagram. The model parameter description is summarized in table 2.1.

Table 2.1: Parameters description of 2HDM+a [17].

Particle	Description
χ	Fermionic DM particle
ϕ_u, ϕ_d	Two Higgs doublets
h, H	Light and heavy neutral CP-even scalars
H^\pm	Charged heavy Higgs
a, A^0	Light and heavy neutral CP-odd pseudoscalar
Parameter	Description
m_x	DM mass = 10 GeV
m_H	Mass of the heavy neutral CP-even scalar
m_h	Mass of the light neutral CP-even scalar, $m_h = 125$ GeV
m_{H^\pm}	mass of the heavy charged CP-even scalar
$\tan\beta$	the ratio of the VEVs of the two CP even Higgs bosons
α	the mixing angle between the CP even scalar Higgs bosons
θ	the mixing angle between the two neutral CP-odd Higgs bosons

CHAPTER 3

The Large Hadron Collider and CMS Detector

The Large Hadron Collider (LHC) is the biggest particle accelerator in the world, located near Geneva on the French-Swiss border. Many key scientific discoveries, such as the discovery of W and Z bosons in 1983[26, 32, 50], the first creation of antihydrogen atoms in 1995[51] and most recently in 2012, the discovery of Higgs boson with mass 125 GeV/c² were made possible by CERN's experiments[52]. The following section describes Large Hadron Collider(LHC), Compact Muon Solenoid(CMS) and its phase-2 upgrade.

3.1 Large Hadron Collider

TThe Large Hadron Collider (LHC) is the biggest particle accelerator in the world[53]. The 27 km long synchrotron storage ring is the final stage of a strong accelerator complex built in the underground cavern of the former Large Electron Positron Collider (LEP). Protons (p) are accelerated within the LHC ring at energy $\sqrt{s} = 13.6$ TeV. The LHC is also designed as to accelerate the lead nuclei (Pb-Pb) at center of mass of energy per nucleons of $\sqrt{s} = 5.36$ TeV for one month each year[53]. Four main detectors of the LHC are CMS, ATLAS, LHCb, and ALICE. They are the main detectors of the LHC, located at four interaction points where two counter-rotating proton beams collide. The particles created in LHC collisions are measured in these experiments. The ATLAS and CMS are used as general purpose detectors that look for new physics by measuring a

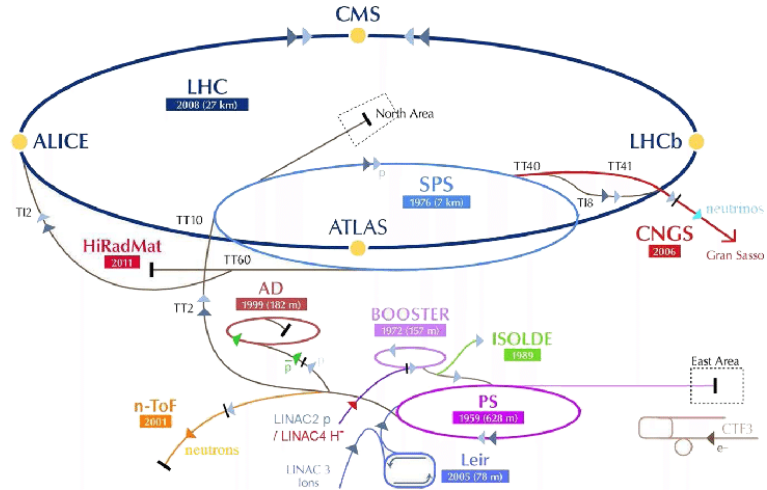


Figure 3.1: A schematic representation of LHC[9].

wide range of new particles. LHCb is mainly looking for CP violations. ALICE study the quark gluon plasma in heavy ion collisions.

Protons are filled into the two counter-rotating beams of the LHC in bunches. One bunch contain 10^{12} protons. There are 2808 bunches in each beam. The proton bunches are held at their circular tracks by 8.33 T magnetic field generated by 1232 superconducting dipole magnets. The beams are focused by 392 quadrupole magnets, with eight radio-frequency (RF) cavities per beam accelerating the particles and ensuring high luminosity[54]. The luminosity L of any particle accelerators which describes the number of collision events per second with a given cross section area. At the end 2018, just before the second long shutdown of the machine, LHC reached the peak luminosity of $2 \times 10^{34} \text{ cm}^{-2}\text{s}^{-1}$. The integrated luminosity since the start of LHC operation was 190 fb^{-1} at the end of 2018. At the end of LHC Run 3, in 2024, that value is expected to reach 350 fb^{-1} [55]. Some key parameters of LHC are given:

3.1.1 The High Luminosity LHC Upgrade

During the LHC's third long shutdown (LS3), which will take place between 2025 and 2027, the accelerator will be upgraded to achieve an instantaneous luminosity of $5 \times 10^{34} \text{ cm}^{-2}\text{s}^{-1}$ and up to $7.5 \times 10^{34} \text{ cm}^{-2}\text{s}^{-1}$. The High Luminosity(HL-LHC) era begins after the LS3 phase. The HL-LHC will collect a total integrated luminosity of 3000 fb^{-1} until 2037. We can easily study the properties of the Higgs boson, rare decay and search for physics beyond the standard model by increasing luminosity. The plan for the future

Table 3.1: The essential real parameters for the LHC are mentioned in the Table.

Parameters	Values
Circumference	27 KM
Number of diploes magnet	1232
Number of main quadrupoles	392
Luminosity	$1.2 \times 10^{34} \text{ cm}^{-2}\text{s}^{-1}$
No of bunches per proton beam	2808
No of protons per bunch	1.2×10^{11}
Energy	6.5 TeV
Number of collisions per second	1 billion
Bunch Spacing	25 ns

high luminosity upgrade is included in the LHC project schedule are given in the figure 3.2.

3.2 Compact Muon Solenoid

Two general-purpose detectors were created for the Large Hadron Collider, and one of them is the Compact Muon Solenoid (CMS). It is made for searches that go beyond SM, such those for extra dimensions and DM candidates, as well as for researching SM physics processes (including the Higgs boson). Although CMS and the ATLAS experiment have similar scientific objectives, they employ different technical approaches and magnet systems. The CMS's structure and functionality are described in the sections that follow.

3.2.1 CMS Detector Design

The CMS detector layout is a cylindrical barrel shape around the beam pipe closed with two endcap disks. It has a total length of 21 m, a diameter of 7.3 m and a total weight of 14,000 ton. It is located in a 100 m underground hall below the village of Cessy in



Figure 3.2: LHC project schedule including the plan for the upcoming high luminosity upgrade.

Figure taken from [10].

France. The detector's name comes from:

- **Compact:** due to the detector's small dimensions compared to its mass and compared to the ATLAS detector's size.
- **Muon:** due to the advanced muon system in the outer layer of the detector.
- **Solenoid:** due to a superconducting solenoid magnet.

CMS has an onion structure, it is a multi-filter with different layers, where each layer consists of a subdetector designed to stop, track or measure different types of particles emerging from proton-proton or heavy-ion collisions. It is split into four major sub-detectors, as seen in Figure 3.3. Three sub detectors are placed inside a superconducting solenoid magnet: the tracking system, the electromagnetic and the hadronic calorimeter. A muon sub-detector is interspersed within an iron magnetic flux return yoke on the solenoid magnet's outside.

These sub-detectors with different materials are used to give information about different particles and measure their energy, momentum and charge and hence identify them. The high magnetic field (3.8 T) from the solenoid magnet provides enough bending power for all the charged particles coming from the collision. The precision measurement of the particle's track curvatures in the tracking detectors helps in identifying the particle's charge and momentum. Photons and electrons produce electromagnetic showers in

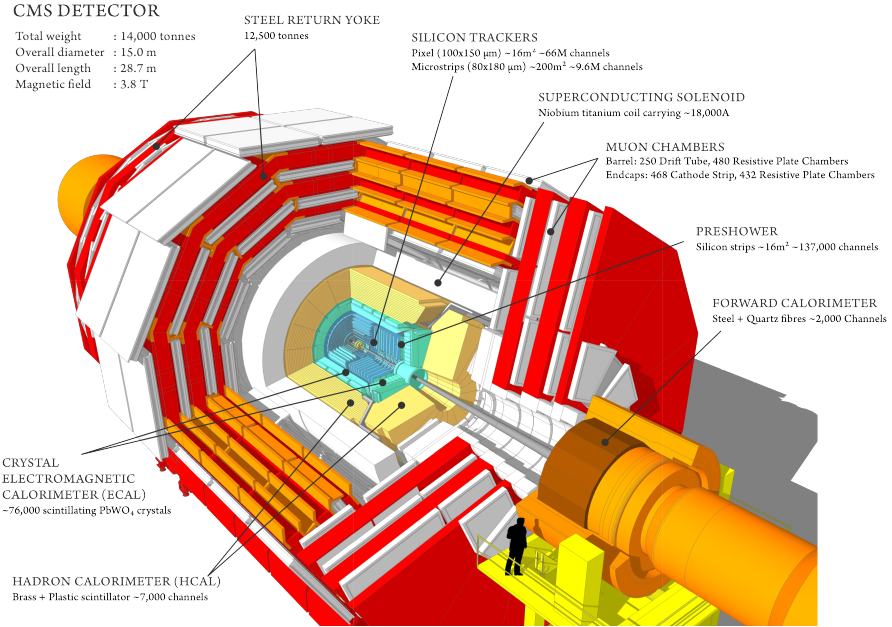


Figure 3.3: A perspective view of the CMS detector [11].

the electromagnetic calorimeter, from these showers the particle's energy is measured. The more penetrating hadrons such as charged pions produce hadronic showers in the hadronic calorimeter, which help in measuring their energy. Muons are the only particles that can traverse all the subdetectors and reach the muon system. Figure 3.4 shows the signatures left when different types of particles pass through the CMS sub-detector. Combining the information from different subdetectors helps in discriminating between particles. As we can see from the figure both photons and electrons leave showers in the electromagnetic calorimeters but photons don't leave tracks in the tracking system and hence we can distinguish photons and electrons. In the same way, we can identify charged and neutral hadrons. Before a description of the sub-detectors, the coordinate system of the experiment must be mentioned.

3.2.2 The CMS Coordinate Systems

In order to explain the detector, the standard coordinate system is defined. At the centre of the detector, the interaction point is taken as the origin of the coordinates. The z-axis is coincident with the anticlockwise beam direction, the x-axis is pointing

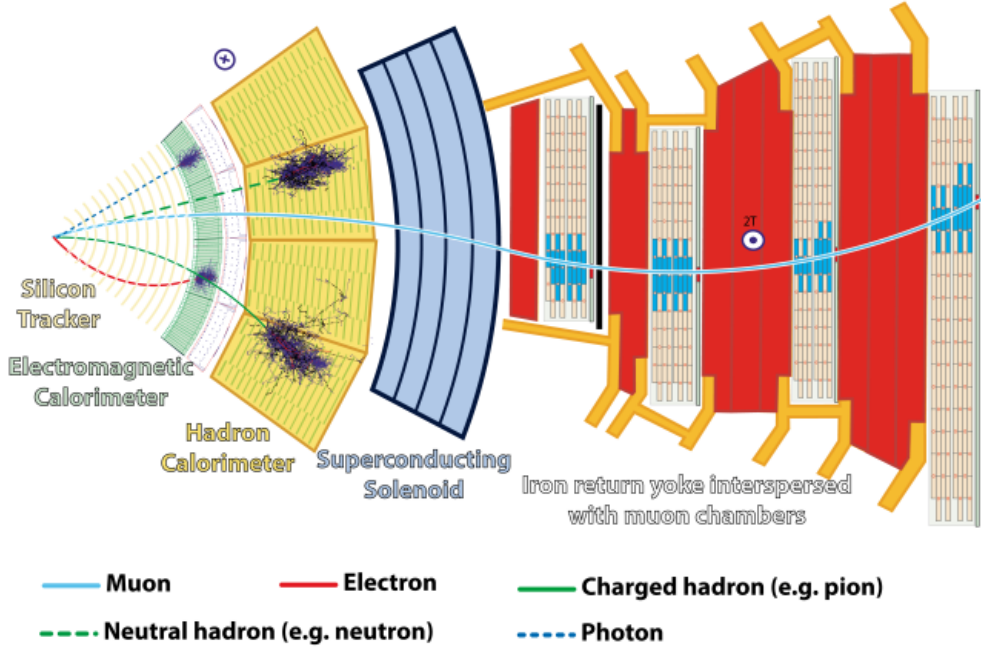
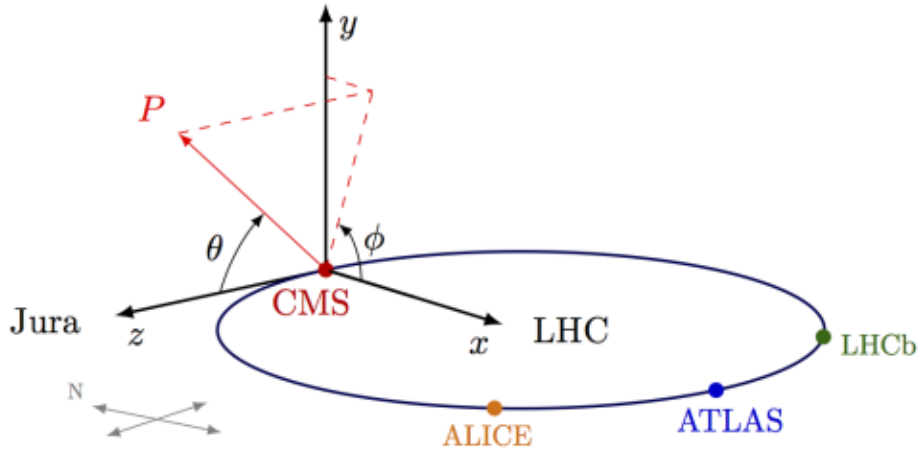


Figure 3.4: The CMS detector transverse section with signatures of different types of detected[12]

towards the centre of the LHC ring and the y-axis is perpendicular to the x-z plane and points vertically upward as shown in figure 3.5. The azimuthal angle called ϕ is defined in the x-y plane such that $\phi = 0$ corresponds to the x-axis directed toward the centre of the LHC ring and takes values of $[-\pi, +\pi]$. The polar angle called θ is defined such that $\theta = 0$ lies along the beam pipe in the positive-z axis and takes values of $[0, +\pi]$. Taking into account that the particles produced by proton collisions are strongly boosted to the collision axis and distributed over the angle θ very unevenly, it is more convenient to use a different kinematic variable called pseudorapidity (η), which is a good approximation of the rapidity of avoiding energy dependence. The η value is determined by Formula 3.2.1:

$$\eta = -\ln \left(\tan(\theta/2) \right) \quad (3.2.1)$$

Smaller (larger) values of η represent the particles lying in a direction perpendicular (parallel) to the beam axis. The distance between two particles is given in terms of a two-dimensional angular distance (ΔR) in the η - ϕ plane and is determined by the

**Figure 3.5:** The CMS coordinate system[13].

Formula 3.2.2:

$$\Delta R = \sqrt{\Delta\eta^2 + \Delta\phi^2} \quad (3.2.2)$$

Another commonly useful variable is the transverse component of the momentum P_T . Before the collision, the parton momentum is expected to be longitudinal (along the beam axis) while the transverse momentum is expected to be negligible. The transverse momentum is particularly useful because the conservation of momentum can be used to quantify an imbalance in the energies of the outgoing particles and hence predict the outgoing particles escaping the detector without leaving signature such as Dark Matter candidate used in this analysis.

3.3 The Tracking System

The silicon tracker is the first sub-detector near the interaction point. Therefore the tracker material must be very resistant to radiation. The diameter of 2.5 m, a total length is 5.8 m and covers a pseudorapidity range of $|\eta| < 2.5$. The tracking system is used to measure with high resolution the charge and momentum of all charged particles as they propagate outward from the collision point while minimizing the energy loss that the particles experience from passing through matter. The tracker can reconstruct the trajectory of all the charged particles coming from the collision point besides the

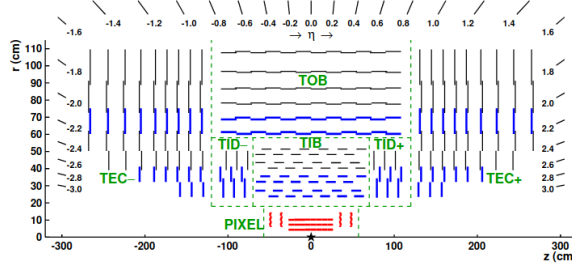


Figure 3.6: CMS tracker system[14].

tracks coming from the decay of very short-lived particles, allowing the identification of primary and secondary vertices with very high resolution [56]. The tracking system is divided into a silicon pixel sub-detector at the inner radius and a silicon strip sub-detector at the outer radius. Figure 3.6 provides a comprehensive overview of the CMS tracker system and its four subsystems: Pixel, Tracker Outer Barrel (TOB), Tracker Inner Barrel (TIB), and Tracker Endcaps (TEC).

Tracker consist of two parts:

3.3.1 Silicon Pixel Detector

Pixel tracker has the capability of correctly reconstructing both primary proton proton interaction vertices and secondary vertices associated with decay of large particles such as b-hadrons. There are 2 endcaps and a barrel region in the silicon pixel detector [57]. Ahead from the beam axis, there are three barrel layer in pixel detector, each with a radius 4.4 cm, 7.3 cm and 11 cm respectively. Approximately, there are 66 million channels in the Pixel detector covering the surface area of 1 m^2 . The schematic diagram of the Silicon pixel detector as shown in figure 3.7[15].

1184 pixel sensor modules are mounted in the pixel detector's barrel region. Approximately radial distance ranging from 300mm to 160 mm from point of collision and 548.8 mm is the length from which the collision is located. An individual module contains a sensor with a resolution of 6650 pixels and a measurement area of $100 \mu\text{m} \times 150 \mu\text{m}$ [58].

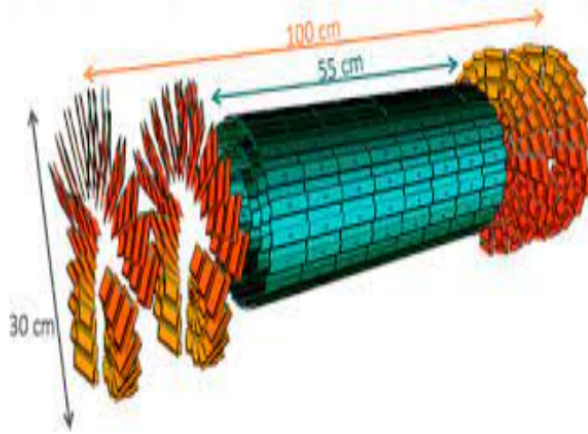


Figure 3.7: Schematic diagram of the Silicon pixel Tracker[15].

3.3.2 Silicon Strip Detector

Silicon strip detectors with 10 million channels surround the inner pixel detector. The barrel region and endcaps of silicon strip detectors are similar to those found on pixels. As for the barrel region, the tracker silicon strip consists of ten layers and nine layers on each endcap of the detector. According to figure 3.8, it is composed of four parts[59]:

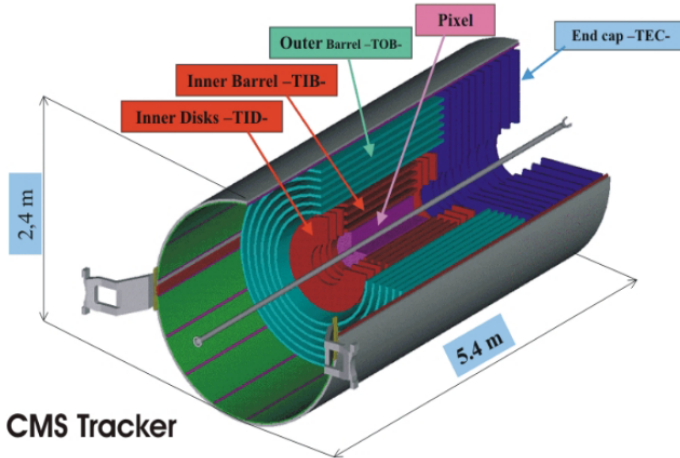


Figure 3.8: Mechanical layout of the pixel and strip tracker[16].

The Silicon Strip detector has a surface area of 198 m^2 , making it the largest silicon tracker ever made[60]. The tracker inner barrel has 4 cylindrical layers that are expanded from "-700 mm to +700 mm" in the "Z" direction and have a radial distance of 255 mm, 339 mm, 418.5 mm, and 498 mm by beam axis. The inner most two layers

contain double-sided modules having strip pitch $80 \mu m$, while the outer most two layers contain single-sided modules having $120 \mu m$ strip pitch.

3.4 The calorimetry sub-detectors

The calorimeter sub-detector lies next to the tracking system and is still within the solenoid magnet. These detectors are designed to measure the energy of both neutral and charged particles. It measures the energy lost by incident particles due to interactions with the detector material which helps in the identification of the incident particle based on the depth of penetration into the calorimeters and the profile of the energy lost. However calorimeter can't detect neutrinos which escape the detector, but their presence can be inferred as an apparent energy imbalance in the collision. The CMS detector includes three calorimetry sub-detectors: The first is a detector called an electromagnetic calorimeter, which measures the energies of electrons and photons. The second detector is called a hadronic calorimeter (HCAL), which measures the energies of hadrons. The third is a detector is called a forward calorimeter, which is made to measure the energies of particles in the detector's very forward regions.

3.4.1 Electromagnetic Calorimeter

The Electromagnetic Calorimeter (ECAL) provides very precise energy measurements. ECAL is the only sub-detector providing information about photons which necessary for the analysis of the $H \rightarrow$ decay. The ECAL is also used in electron reconstruction: the combination of its information with the tracker provides a very precise measurement of electron position and energy necessary to analyse the multi-lepton final state.. Electromagnetic showers are created when these particles make interaction with the calorimeter material while depositing the whole energy. As a result, the particles in the calorimeter have come to rest. The crystals of Lead Tungstate ($PbWO_4$) act as a scintillator in ECAL, which are read out by an avalanche photodiode. The scintillator's light output is proportional to the deposited energy.

The ECAL provides a pseudorapidity coverage of $|\eta| < 1.479$ in the barrel which is called

the ECAL Barrel (EB), and to $1.479 < |\eta| < 3.0$ in the endcap region named ECAL Endcap (EE). Figure 3.10 shows the ECAL barrel and an ECAL endcap may be seen in a longitudinal image of a portion of the CMS electromagnetic calorimeter, with the preshower in the front.

A preshower (ES) detector is installed in front of the ECAL endcaps in the forward region of the detector to differentiate between single photon emission and photons coming from the pion $\pi^0 \rightarrow \gamma \gamma$ decay to two photons very close to each other.

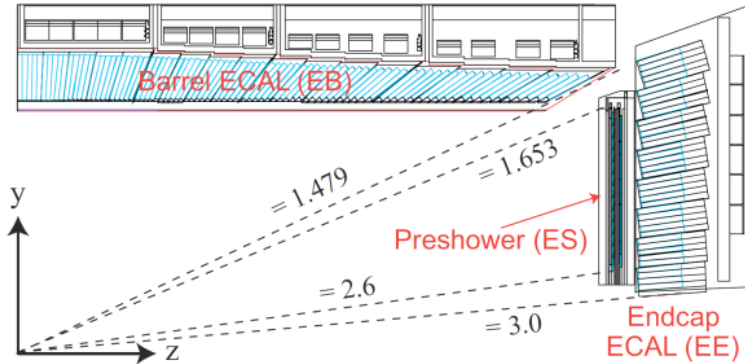


Figure 3.9: The ECAL barrel and an ECAL endcap may be seen in a longitudinal image of a portion of the CMS electromagnetic calorimeter, with the preshower in the front. [17].

3.4.2 Hadronic Calorimeter

The hadronic calorimeter (HCAL) [18] is located Between the ECAL and the interior of the solenoid magnet. Its purpose is to measure the hadronic jets' energy and location. Figure 3.11 illustrates the three parts that make up the HCAL: the HCAL Barrel detector (HB), the HCAL End-cap detector (HE), and the HCAL Forward detector (HF). The thick brass used in HCAL serves as the absorber while the active component is a plastic fluorescent scintillator. A hadronic particle's impact on an absorber plate starts an interaction that generates a number of secondary particles. These secondary particles may interact as they pass through more layers of absorber, creating a cascade or "shower" of particles. The particles in this shower emit light as they move between the alternating layers of active scintillation material. The total amount of light energies emitted by the scintillator along the route of the particle is then used to calculate the energy of the particle.

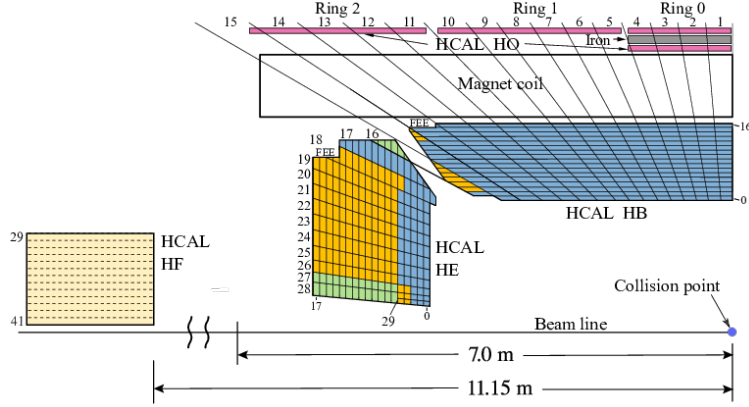


Figure 3.10: An overview of one-quarter of the CMS HCAL showing the four major components: the hadron barrel (HB), the hadron endcap (HE), the hadron outer (HO), and the hadron forward (HF) calorimeters.[18].

3.5 Solenoid Magnet and Iron Return Yoke

A huge superconducting solenoid magnet generates a 4 T magnetic field. Trajectories of charged particles bent by the magnetic field. Those particles that have more bending have less momentum and vice versa. The magnet's iron return yoke alone contributes 12500 tonnes to the whole detector weight of 14000 tonnes. Iron return yokes are used for the structure building of CMS and as magnetic field absorbers.

3.6 Muon Chamber

The CMS muon chambers are built into the magnet's iron return yoke. Gaseous detectors used in muon chambers include drift tubes, resistive plate chambers, and cathode strip chambers. The function of these detectors is to measure the position and momentum of muons. The muon system keeps the CMS detector hermetic for all particles except neutrinos, and so plays important role in the indirect detection of neutrinos via missing transverse energy. The schematic diagram of CMS illustrating various sub-detectors as seen in Figure 3.12.

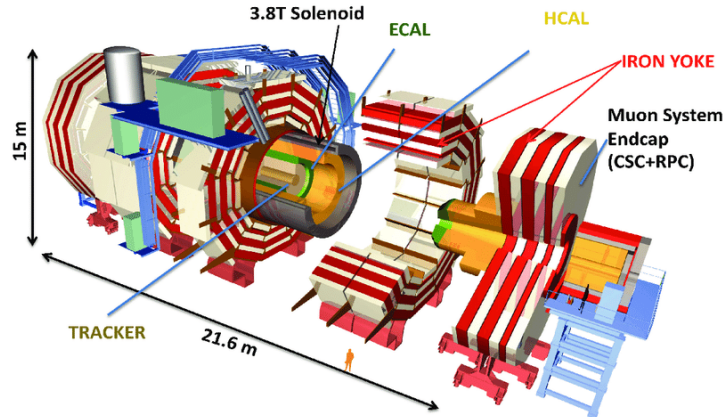


Figure 3.11: Drawing illustrating the various sub-detectors of the CMS experiment[19] .

3.7 Trigger Concept

In CMS, there are two trigger stages that lower the data production rate and choose events with a high physical interest for storage. The Level L_1 is a hardware trigger that reduces data from 40 MHz to 100 kHz. The level L_2 stage is a software trigger that further reduces the data to 1 Hz[61].

3.8 The CMS phse-2 Upgrade

Between 2025 and 2027, the CMS Phase-2 Upgrade will take place, preparing the complete CMS detector for the requirements of the HL-LHC environment. The new detector must be able to tolerate high amounts of radiation, have the greater granularity to cope with a pileup of 140, have larger bandwidth to get larger data rates and have improved trigger performance. The muon system will improve the current gas detectors. In the forward region, gas electron multiplier detectors will be installed. The replacement of the HCAL hybrid photodiode readout with silicon photo multipliers (SiPM) in ECAL and HCAL is included in the phase 2 upgradation. The CMS silicon tracker and the calorimeter endcaps, in contrast to the other sub-detectors, will experience extensive upgrades. By 2024, the CMS tracker will have suffered significant radiation damage and will need to be replaced completely. Similarly, at above 500 fb^{-1} , the existing forward calorimeter will not be able to maintain appropriate performance and will be replaced by the High Granularity Calorimeter (HGCAL).

3.8.1 Tracker Upgrade

Increased radiation hardness, an improved layout, a new module design in the Outer Tracker that allows its contribution to the L_1 trigger, a decreased material budget, and longer forward coverage are all features of the new CMS tracker[62]. It is further divided in two sub-detectors:

The small pixel detectors are included in the inner tracker, and silicon macro-pixel detectors and strip detectors are included in the outer tracker.

Tracker Layout and Sensor Modules

The updated tracker's layout is designed to provide robust tracking and expanded forward coverage while keeping the material budget low. The Inner Tracker has four barrel layers and twelve discs on each end, providing forward coverage of up to $\eta = 4$. A total active area of 4.9 m^2 is covered by the pixel modules. The Outer Tracker is made up of six barrel layers and five discs on each end. The outer tracker comprises of two types of modules. Modules consisting of a silicon macro-pixel sensor and a silicon strip sensor are called "PS modules" in the inner regions of the Outer Tracker. The outer-layer modules are referred to as "2S modules" since they are made up of two silicon strip sensors.

In the $r - z$ view, four parts of the CMS Tracker layout are shown. The Inner Tracker's pixel modules are coloured green (with two readout chips) and yellow (four readout chips). The Outer Tracker has modules with two strip sensors (2S, red) and modules with one strip sensor and one macro-pixel sensor (PS, blue) as shown in the 3.13 figure that allows for track discrimination with low transverse momentum.

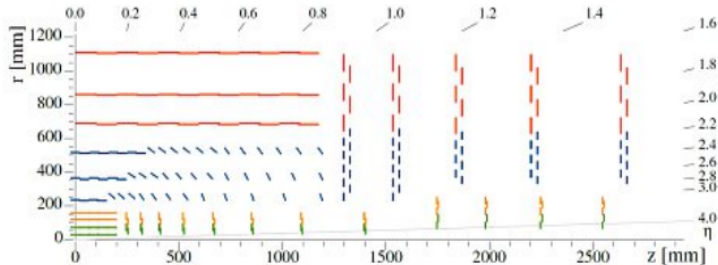


Figure 3.12: One fourth segment of the CMS Phase-2 tracker[20].

3.8.2 Trigger Input

The Outer Tracker's PS and 2S modules are designed to allow transverse momentum (P_T) discrimination at the module level. Both types of modules comprise two closely stacked, parallel oriented sensors. The special readout chips correlate the hit positions on both sensors of each module to calculate the particle P_T . Stubs are tracks that fall within the search window and have a P_T threshold of 2 GeV. Stubs are sent to the Outer Tracker's back-end electronics at bunch crossing frequency, where they are processed into specific tracking algorithms that reconstruct tracks. The threshold frequency for L_1 trigger decision is 750 kHz.

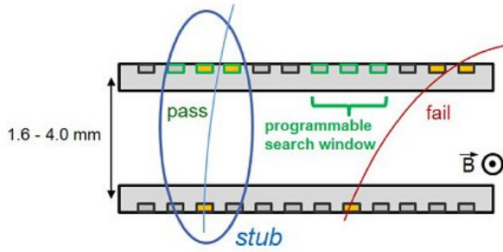


Figure 3.13: p_T -trigger modules[21].

3.8.3 High Granularity Calorimeter

HGCAL will have a high radiation tolerance, precise timing of high energy showers, and contributed L1 trigger decision. HGCAL is a calorimeter which uses silicon sensors and scintillating tiles as active material. It is divided into two sections: an electromagnetic compartment (CE-E), which uses silicon as an active material, and a hadronic compartment (CE-H) which use both silicon and plastic scintillators which are read by SiPMs. CE-E uses copper, copper-tungsten, and lead plates as an absorbing material wrapped in stainless steel, while CE-H uses stainless steel. The entire volume calorimeter is thermally insulated and kept at a constant temperature of 35 °C. Hexagonal p-type sensors are the silicon base material for HGCAL, and they come in two granularities and three thicknesses (300 μm , 200 μm , and 120 μm) to allow for regions of variable fluence inside the detector volume. The maximal fluence values for the 300 μm , 200 μm , and 120 μm thick sensors, respectively, are $5 \times 10^{14} \text{ neq/cm}^2$, $2.5 \times 10^{15} \text{ neq/cm}^2$, and $7 \times 10^{15} \text{ neq/cm}^2$.

$n_e q/cm^2$ at an integrated luminosity of $3000 fb^{-1}$. Silicon is used in high-fluence areas of the calorimeter, while scintillators are used in lower-fluence areas. Silicon covers approximately $620 m^2$. More detail of the HGCAL of the silicon sensor is seen in Figure 3.15:

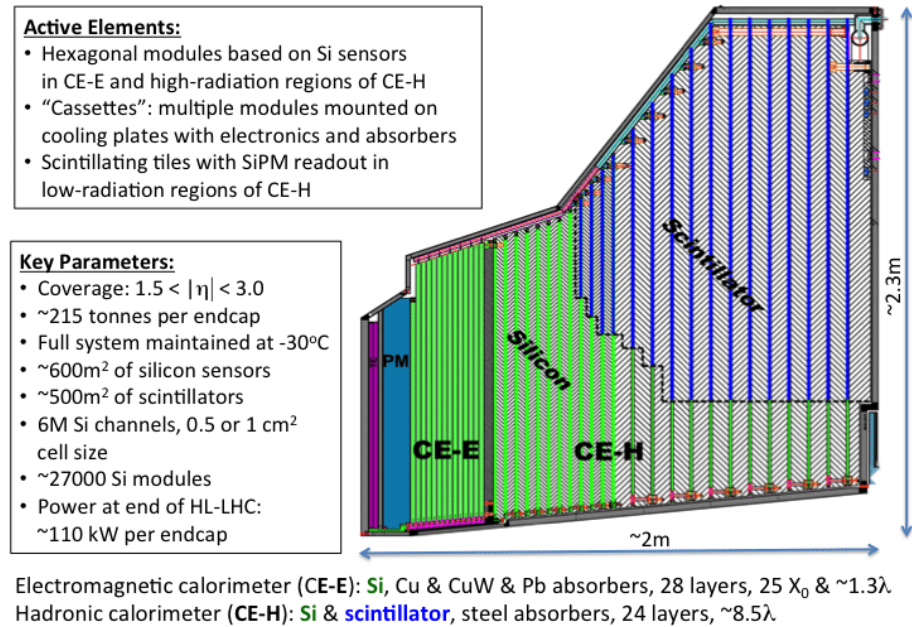


Figure 3.14: Cross section of CMS HGCAL. Figure 3.17 taken from[22].

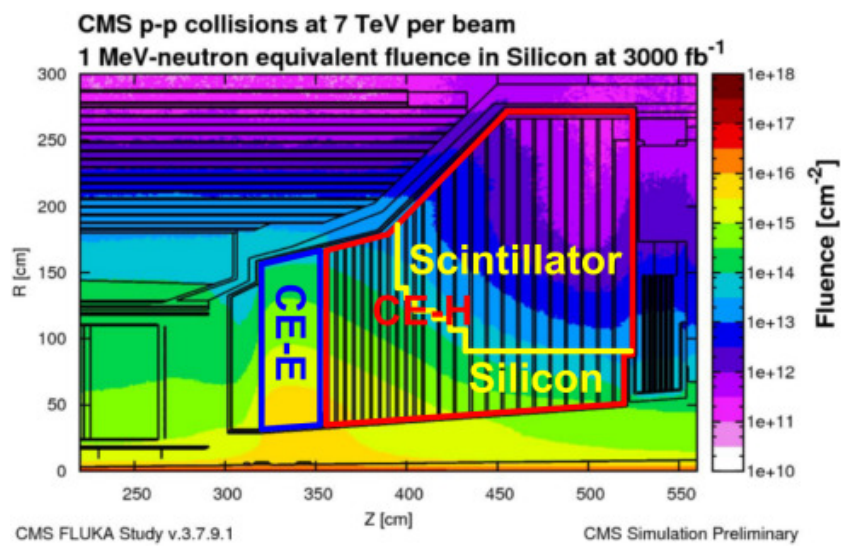


Figure 3.15: FLUKA simulation of the particle fluence in $1\text{MeV}n_{eq}/\text{cm}^2$ accumulated in HG-CAL after an integrated luminosity of 3000fb^1 . The layout is shown in r-z view. Figure 3.16 taken from [20].

CHAPTER 4

Simulation and Analysis Tools

4.1 Events Generators

The generation of events is the first step of the simulation process which uses the Monte carlo (MC) technique to simulate events similar to the real experiments. At LHC, the protons are accelerated at very high energies and then collide. The interaction takes place between the proton constituents “the partons”, which is a term that globally indicates quarks and gluons inside the proton. In each collision, not all the interactions produce high energy particles. However, sometimes two partons from separate protons interact very strongly and produce an interesting event for the study. The types of interactions that can take place in the collision are shown in Figure 4.1 and are described below [63]:

- **Hard Scattering:** Hard processes resulting from the interaction between the constituents of two colliding protons having high momentum exchange between them and having product particles with high momentum in the perpendicular direction to the protons’ the original direction of motion. In the event generation process, the incoming and outgoing partons of the hard scattering process may also emit initial and final state radiations, called Parton Showers (PS).
- **Underlying Events:** As a result of this soft scattering process, proton remnants that did not participate in the hard scattering process are involved in the scattering process. In addition to soft scattering between these partons (known as Multiple Parton Scattering), they may also radiate gauge bosons prior to or after colliding, referred to as initial state radiation (ISR) and final state radiation (FSR). As a result of FSR and

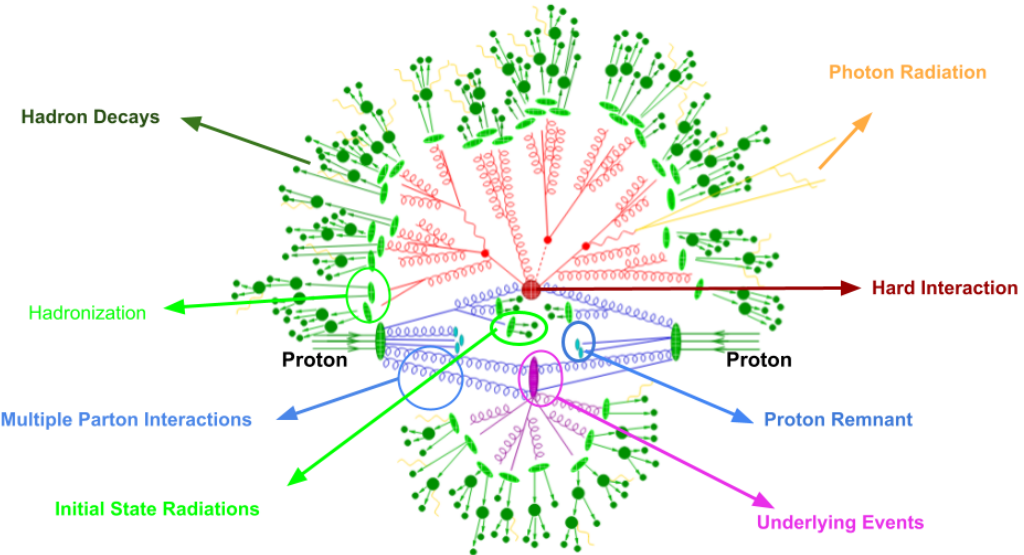


Figure 4.1: Monte-Carlo simulations of LHC Collisions[23]

ISR, jets are created near the direction of incoming and outgoing hadrons.

- **Pileup Process:** In the LHC, bunches of protons are accelerated and collided and each bunch contains 10^{11} protons. Pileup refers to any interactions that happen between protons which were not involved in the hard scattering within the bunch crossing.
- **Hadronization:** After the interaction, the process of combining quarks and gluons forming colorless hadrons that are observed in the final state is known as the hadronization process. This process happens when the partons reaches to the hadronization scale of ≈ 1 GeV. In terms of the transition from a colored partonic system to a colorless partonic system, there are two models:
 - The Cluster Model: In this model, gluons are split into $q\bar{b}$ pairs where quarks are clustered together into colorless groups. Clusters formed in this way have large invariant mass which further decay to smaller mass scales suitable to form hadrons [64].
 - The String Model: In this model, gluons are split into quarks, the produced quark and antiquark move out in opposite directions from their production vertex and lose their energy. During the motion, a string like configuration between them is formed. When a string is stretched, the potential energy stored in the string increases and the kinetic energy decreases, which breaks the string into two parts forming $q\bar{q}$ pairs. The process is continued till the energy left to create another such pair is very low [65].

The CMS Collaboration uses different MC event generators to generate physics processes for different purposes such as PYTHIA [66], Madgraph [67] and POWHEG [68].

4.2 Event Generation at Parton Level

For the event generation, we are using Madgraph, which is a matrix element generator and a phase-space sampler. We need to provide Madgraph with the 2HDM+a [69] model for our analysis in a Universal FeynRules Output (UFO) format. This UFO file contains the Lagrangian and all relevant Feynman rules with all physical parameters. It generates a matrix element, the corresponding diagrams and the helicity amplitude with ALOHA. With the resulting code, the matrix elements can be evaluated at a given phase space point. The Feynman diagrams for the processes are obtained by considering all possible combinations of external particles and if there are vertices in the UFO allowing the final state particle combinations, the diagram is saved in an output file.

ALOHA creates routines for helicity amplitudes to calculate the matrix element. The advantage of helicity amplitudes is that it is a convenient and effective way to compute the matrix element squared, because it works at the amplitude level, while the trace method, which is based on completeness relations, works on a squared amplitude level. By using helicity amplitudes, the complexity grows only linearly and diagrams can be factorized. This leads to faster computations compared to the tracing technique. All helicity amplitudes from every diagram can be summed and squared to yield the overall result.

The total cross section of the process is computed with the Monte Carlo integration of the squared matrix element. Because the integrals cannot be solved analytically, Thus solved numerically. The phase-space points required to solve the integral are generated according to a distribution which is not exactly the real distribution describing the parton-level events. To compensate for this, a weight is assigned to each point, corresponding to their contribution to the real distribution. Madgraph then performs an unweighting procedure to turn the weighted samples into unweighted ones. The Parton distribution functions(PDFs) NNPDF30_lo_as_0130 [70] and NNPDF23_lo_as_0130 [71] are used for mono-Z and mono-Higgs analysis respectively.

4.3 Parton showering and hadronisation

The next step in the simulation chain is PYTHIA, which uses the four momenta from incoming particles and simulates the parton shower and the hadronization process.

The free partons, which consists of quarks and gluons, out of the initial process, can radiate a single gluon. These gluons can again radiate another $q\bar{q}$ pair or a gg pair if they are highly energetic and these quark and gluon pairs still have enough energy, they can radiate yet another quark or gluon pair and so on, as long as they have a sufficient amount of energy. At the LHC, we can see the showers induced by the processes as jets. The shower evolution in PYTHIA is based on DGLAP splitting kernels $P(z)$, describing the probability that for example a single parton will split in two with an energy fraction z . These splitting kernels $P(z)$ are derived.

Then hadronisation takes place on a low-energetic non-perturbative scale. There the single partons from the showering process are grouped together in order to form hadrons. The basic principle behind hadronisation is the concept of color confinement, so only color-neutral states can exist. In order to simulate hadronisation processes, a Lund string framework is used in PYTHIA. Color confinement can be modelled by a color flux tube, forming between particles with color. When the distance between two particles increases, the force between the particles grows linearly and the energy decreases for the color dipole. At some point the energy is too high and the color flux tube breaks and produces a new $q\bar{q}$ pair with the energy stored in the tube. If there is enough energy available new $q\bar{q}$ is produced. At some point only on-shell particles can be produced and the process of hadronisation stops. Unstable hadrons decay into stable hadrons, for example pions and other particles decay accordingly to the decay channels implemented in Madgraph or PYTHIA. The output file of PYTHIA contains all the information from showering and hadronisation, including the mother and daughter particles, the four-momenta of the particles, their status (at which point in the process the particle was created), particle ID and color state. These hadrons and other remaining particles are now passed on to the detector simulation

4.4 ROOT

In high energy physics, a framework called ROOT [72] is utilised to evaluate huge amounts of data. It uses the C++ format language. In addition to using histograms and graphing to analyse and visualise the data, curve fitting, functional minimization, statistical tools for data analysis, matrix algebra, four-vector computation, common mathematical functions, 3D visualisations (geometry), and interface Monte Carlo event are just a few of the cool packages that ROOT has to offer. A crucial component of ROOT is a data container known as a tree, which has branches and leaves substructure. ROOT is used for data analysis by a large number of experiments, including BaBar, CDF, PHENIX, and upcoming detectors including ALICE, ATLAS, CMS, and LHCb.

CHAPTER 5

The mono-Z($\ell\ell$)+ E_T^{miss} Analysis

This chapter provides detail on the mono-Z($\ell\ell$)+ E_T^{miss} analysis, which was performed using MadGraph5_aMC@NLO (MadGraph5 is a software package that is used to generate Feynman diagrams, which are graphical representations of mathematical equations that explain the interactions of particles. The aMC@NLO (Automatic Multi-Channel @ Next-to-Leading Order) extension to MadGraph5 allows for the calculation of higher-order corrections to these predictions, which can improve the accuracy of the results) at $\sqrt{s} = 13$ TeV. Two Higgs Doublet Model + Pseduscalar is used for this analysis:

- 2HDM+a (discussed in detail in section 2.6.1) can produce several mono-X signatures. A signature where mediator 'a' is resonantly produced in association with the SM particle X. Then 'a' decays into a dark matter pair $\chi\chi$ producing a mono-X signal. In this chapter, we will discuss only Z+E T^{miss}

By decaying heavy neutral Higgs (H) to a Z boson and a pseudoscalar 'a', this model produces a mono-Z signal. This analysis examines a signal that consists of two DM particles that are detected in the detector as missing transverse momentum, back to back with boosted Z bosons that decay into two charged leptons, either e^+e^- or $\mu^+\mu^-$. As compared to jets, charged leptons have the advantage that they are relatively easy to reconstruct in detectors. Additionally, a jet veto is used to eliminate the large multijet background. Compared to mono-jet, the mono-Z process has a smaller cross-section (which is a disadvantage).

5.1 Signal samples

The mono-Z ($\ell\ell$)+ E_T^{miss} signal samples have been studied using MadGraph, Parton Distribution Function (PDFs) NNPDF30_lo_as_0130, PYTHIA 8.3 for parton showering, and Pseudoscalar_2HDM UFO model. The gluon gluon fusion is generated using the MadGraph5 syntax

```
MG5_aMC > import model Pseudoscalar_2HDM
```

```
MG5_aMC > generate g g > ℓ+ ℓ- xd xd~ / h1 [noborn=QCD]
```

Here xd and $xd\sim$ are dark matter particles and antiparticles have Particle Data Group IDs are 52 and -52 respectively. The noborn ensures that no tree level contribution will be included and QCD ensures that only color charge particles (quarks and gluons) will participate in the loop.

The mono-Z signal can also be produced by $b\bar{b}$ fusion. The MadGraph syntax used to generate the $b\bar{b}$ fusion process is

```
MG5_aMC > import model Pseudoscalar_2HDM - bbMET_5FS
```

```
MG5_aMC > generate p p > ℓ+ ℓ- xd xd~ / h1 a
```

In this case, the contribution from an intermediate Higgs or photon is removed.

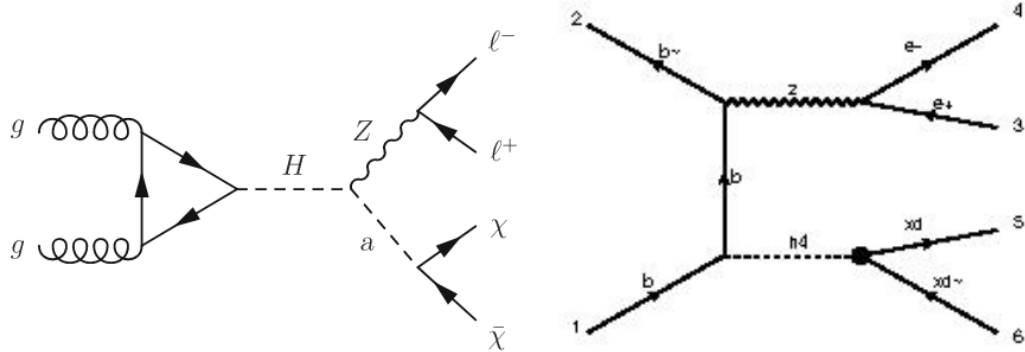


Figure 5.1: A Feynman diagram shows the final state of the Z boson produced by the 2HDM+ model, which decays into a pair of leptons and a pseudoscalar "a" which decay into pair of dark matter. (right) $b\bar{b}$ fusion, here $h4$ represent pseudoscalar a , (left) gg fusion

5.2 Standard Model Background Processes

Apart from potential DM signals, SM processes can also result in a mono-Z($\ell\ell$) signature. The dominant backgrounds in this analysis are ZZ, Z+jets, WW, t \bar{t} , WZ, W+jets. These backgrounds are estimated from MC simulation. Compared to the final state of the signal.

5.2.1 t \bar{t} production

As shown in Figure 5.2(top left), top quark pair production (t \bar{t}) contributes mainly to the background due to leptonic decays. Each top quark decays to a b-quark and a W-boson. W boson further decays into charge leptons and neutrinos. neutrinos leave the detector without interaction like potential DM particles, their presence can only be indirectly inferred from E_T^{miss} . As a result, leptonic decay of t \bar{t} can produce a mono-Z($\ell\ell$)signature.

5.2.2 Di-Bosons Processes

The production of ZZ and WW di-bosons are the main backgrounds in the mono-Z channel. In the ZZ process, one Z boson decay to $\ell\ell$ while the other Z boson decay to $\nu\nu$. On the other hand, in the WW process, one W decay to $\ell\nu$ and the other W also decays to $\ell\nu$ as shown in Figure 5.2 (top right). These are simulated at leading order.

5.2.3 V+Jets

Figure. 5.2 (bottom row) shows the Feynman diagram for the production of the vector bosons (Z, W) plus jets: The Z-boson decays into two neutrinos and leaves a significant amount of energy behind. Also, W decays to neutrino and charge lepton which also produces some missing energy. but missing energies in V+jets are small compared to the signal (simulated at parton level).

5.3 Variations of Parameter

To choose the best value for the analysis, we did scans for $\sin\theta$, $\tan\beta$ and m_χ .

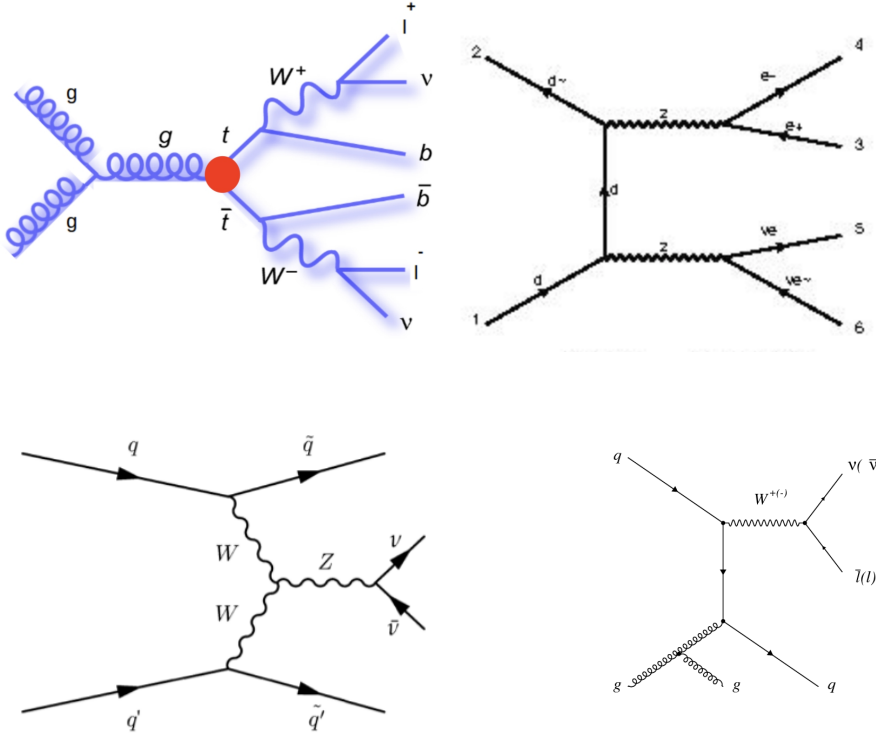


Figure 5.2: Feynman diagrams shows the background $t\bar{t}$ (top row left), ZZ (top row right), $Z+\text{jets}$ (bottom row left), and $W+\text{jets}$ (bottom row right)

5.3.1 Variation of $\sin\theta$

In the $Z+E_T^{miss}$ channel, the heavy neutral Higgs (H) decay to a Z boson and pseudoscalar a , and the relevant coupling scale is $g_{HZA} \propto \sin\theta$, it means that the mono- Z signal will vanish in the limit of $\sin\theta \rightarrow 0$. The mixing angle among the two neutral CP odd Higgs bosons is θ . we choose different values of $\sin\theta$ and plotted against the cross-section as shown in Figure 5.3 (left).

Figure 5.3 (right) shows E_T^{miss} distributions in $Z + E_T^{miss}$ production for different values of $\sin\theta$. The masses of spin 0 particles are set to $M_a = 400$ GeV and $M_A = M_H = M_{H^\pm} = 700$ GeV. Other parameters are set to (2.6.3). The distribution shows that the modification of $\sin\theta$ leads in a change of the total cross-section only but the shape does not change. For better sensitivity of signal, we can choose $3.5 \leq \sin\theta \leq 0.7$.

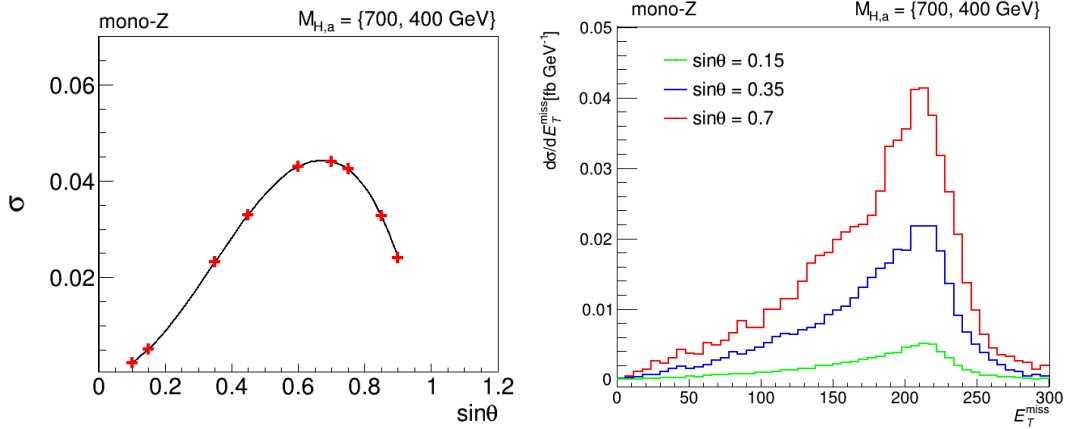


Figure 5.3: E_T^{miss} distributions for mono-Z production for various values of $\sin\theta$. Other parameters are set to (2.6.3) using $M_a = 400 \text{ GeV}$ and $M_A = M_H = M_H^\pm = 700 \text{ GeV}$.

5.3.2 Variation of $\tan\beta$

$\tan\beta$ is defined as the ratio of two CP-even Higgs bosons' Vacuum Expectation Values (VEVs). We choose different values of $\tan\beta$ and plot them against the cross-section as seen in Figure 5.4 (left). As we can see in the figure, as the value of $\tan\beta$ is increasing, the cross-section is decreasing, that's why we chose $\tan\beta = 1$ in the benchmark parameters. The E_T^{miss} distribution in mono-Z production for various $\tan\beta$ values is shown in Figure 5.4 (right). From the distributions, it can be shown that the shape of the distributions are less affected by changes in $\tan\beta$ for the parameters $M_a = 200 \text{ GeV}$ and $M_A = M_H = M_H^\pm = 700 \text{ GeV}$.

5.3.3 Variation of m_χ

The m_χ is a DM particle mass. By varying the value of m_χ we came to know for which value we can get better signal sensitivity. in Figure 5.5 (left), we can see that the cross-section is almost the same for $m_\chi \leq 100$, which is why we choose $m_\chi = 10 \text{ GeV}$.

The modifications of the E_T^{miss} spectrum in $Z + E_T^{miss}$ production under a variation of m_χ are shown in Fig. 5.5 (right). The given distributions correspond to the benchmark parameters in (2.6.3) with $M_a = 300 \text{ GeV}$, and $M_A = M_H = M_H^\pm = 700 \text{ GeV}$. The green and blue histograms correspond to the scenario with $M_a > 2m_\chi$ lead to almost identical rates of E_T^{miss} spectra. while the red histogram corresponds to the scenario where $M_a < 2m_\chi$ which is kinematically not allowed that's why the cross-section is reduced and

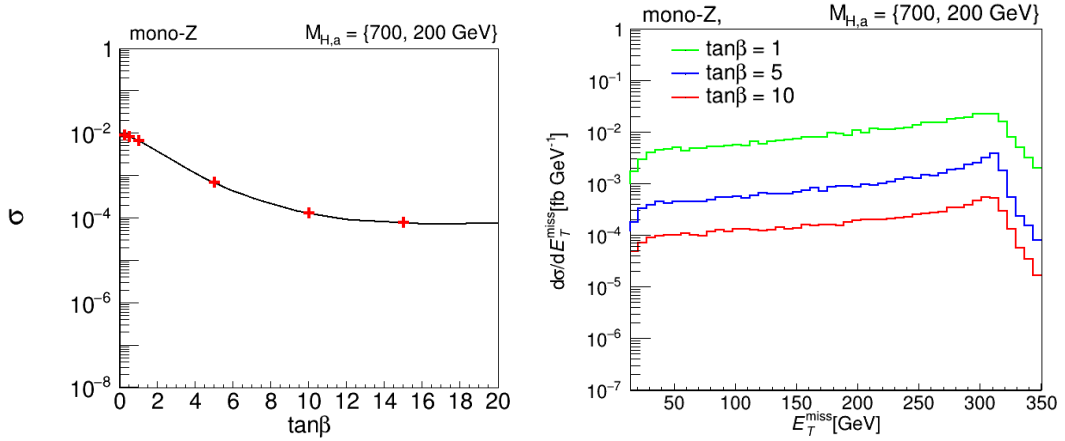


Figure 5.4: The distribution shows that for $\tan\beta \leq 1$, we have maximum cross-section (left). E_T^{miss} distributions for mono-Z production (right). The 2HDM + a parameters are set to (2.6.3) using $M_a = 200 \text{ GeV}$ and $M_A = M_H = M_H^\pm = 700 \text{ GeV}$.

the shape is also changed.

5.4 Missing Energy

To search for DM, one approach is to detect its interactions with ordinary matter in order to find evidence of its existence. In particle collision experiments, one way to do this is to look for missing energy, i.e., the total energy of the particles involved in a collision is not equal to that of the particles detected after the collision. There is a possibility that some of this energy could be carried away by invisible dark matter particles.

In this analysis, we have studied a mono-Z channel in which a single particle, a Z boson is produced in the collision. We are looking for missing energy in this channel as a possible signature of dark matter. In order to gain insight into the nature of dark matter and its role in the universe, we hope to study the properties of the missing energy and the particles involved in the collision.

But the standard model background also produced missing energy. we applied missing energy cuts to reduce the SM background as shown in Table 5.1.

On the SM background and the signal, the same missing energy cuts have been applied

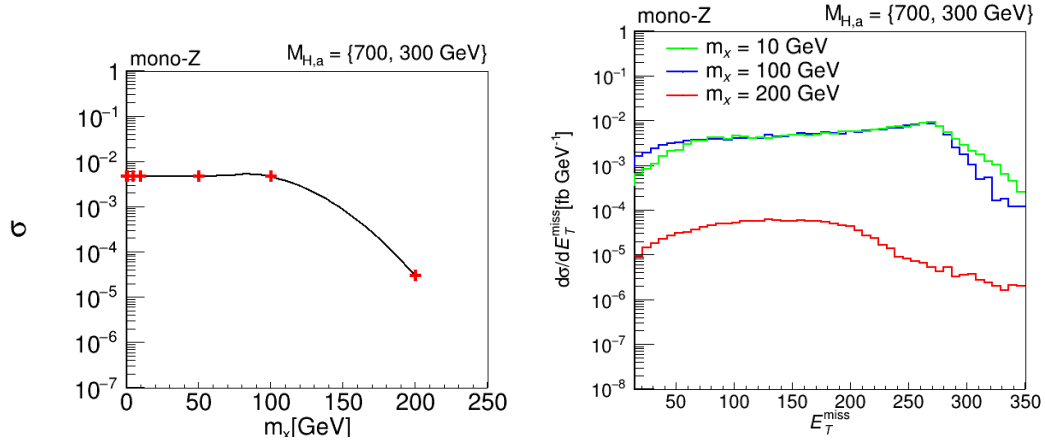


Figure 5.5: E_T^{miss} distributions for mono-Z production. The distribution corresponds to different values of m_χ . Other parameters are set to (2.6.3) using $M_a = 300$ GeV and $M_A = M_H = M_H^\pm = 700$ GeV.

Process	Cross Section(pb)	Missing Energy (GeV)				
		100	150	200	250	300
ZZ	0.2495	0.031	0.010	0.003	0.001	0.0008
WW	3.06	0.02	0.003	0.008	0.0002	0.0001
$t\bar{t}$	23.14	5.12	0.84	0.174	0.05	0.01
Z+ jets	51.86	5.96	1.61	0.53	0.20	0.08
Total	78.3	11.11	2.46	0.70	0.25	0.09

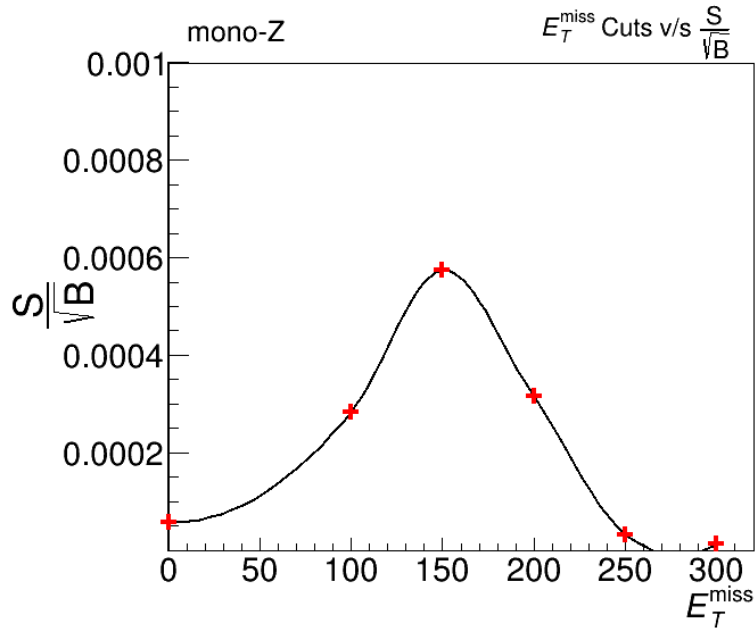
Table 5.1: The SM background in the signal region.

as shown in Tables 5.1 and 5.2.

5.4.1 Signal Significance

In order to observe the signal over the background, experimentalists quote a quantity S/\sqrt{B} 'S' represents the number of "signal events" and 'B' represents the number of "background events". if $S/\sqrt{B} = 5\sigma$, one can claim the presence of a signal. Figure 5.6 shows that the significance of a signal is high at missing energy cut = 150 GeV.

Process	Cross Section(Pb)	Missing Energy (GeV)					
		100	150	200	250	300	
Signal	0.004	0.003	0.0014	0.0002	9.8e ⁻⁶	1.8e ⁻⁶	

Table 5.2: Applied energy cuts on the signal.**Figure 5.6:** Significance of a signal.

5.5 Transverse Momentum

A particle's transverse momentum is its momentum perpendicular to the beam direction (z-axis). Mathematical form of transverse momentum is given below:

$$P_T = \sqrt{P_x^2 + P_y^2} \quad (5.5.1)$$

Missing Transverse Energy

All the outgoing particles, "charged and neutral", produced from the collision leave a signature in the detector's material except neutrinos "or hypothetical neutral weakly interacting particles" which leave the detector without interacting. This quantity can be detected by observing the momentum imbalance in the transverse plane (plane perpendicular to the beam direction). The quantity is also known as the missing transverse energy E_T^{miss} or (MET). It is not only important to understand SM physics through

the measurements of the W boson, top quark, and tau lepton decays, where neutrinos are interpreted as the MET, but it is also an important factor in searches for physics beyond the standard model, such as the search for dark matter and supersymmetric particles and extra dimensions, where the MET is interpreted as a new particle due to the existence of hypothetical neutral massive particles with weak weak interactions. In a particle flow (PF) reconstruction, the MET is defined as the negative vector sum of the transverse momentum of all reconstructed particles.

The p_T^{miss} distribution is shown in Figure 5.7, with a peak at about 220 GeV and a range from 0 to 400 GeV. Actually, the dark matter particles that don't interact with a detector carry this momentum.

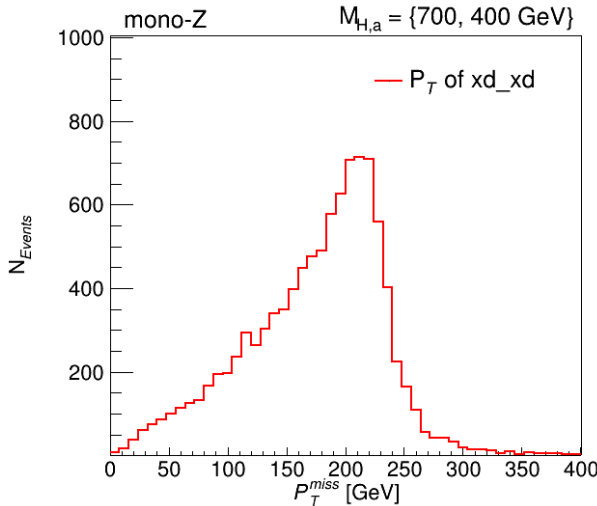


Figure 5.7: Missing Transverse momentum distribution.

The transverse momentum of the Z boson

One Z boson recoils against the missing energy in the signal region. Figure 5.8 shows the p_T distribution for a Z boson with a peak around 220 GeV. The transverse momentum of a signal corresponds to $\sin\theta = 0.7$. The rest of the parameters are set to (2.6.3) using $M_a = 400$ GeV and $M_A = M_H = M_H^\pm = 700$ GeV.

Transverse Momentum of charge leptons of background

In the ZZ background, one Z decay to two neutrinos and the other Z decay to two charge leptons. Figure 5.9(left) shows the transverse momentum of Z decayed to charge leptons. The $t\bar{t}$ decay fully leptonically, so we have opposite charge leptons in final state. Figure

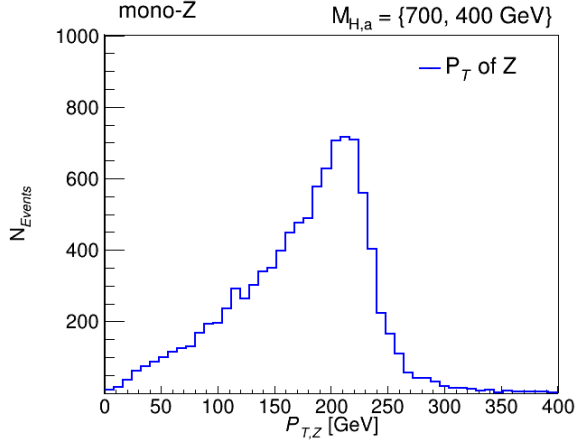


Figure 5.8: P_T distribution of Z boson.

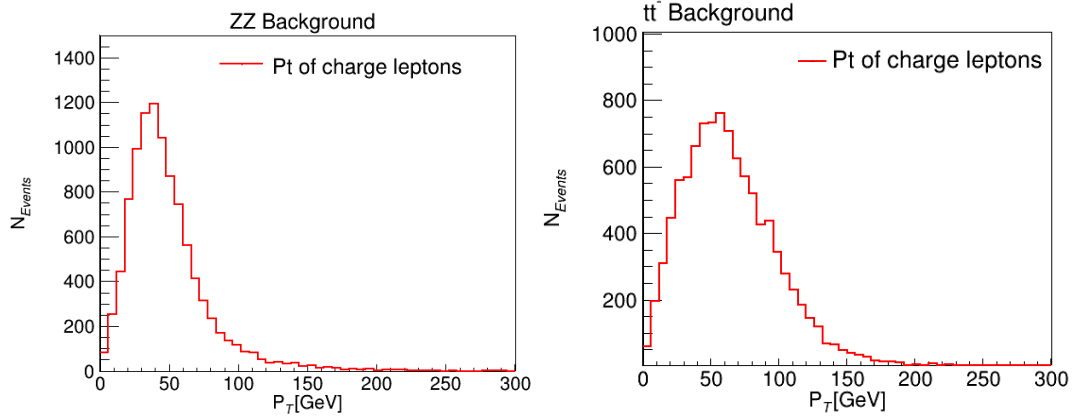


Figure 5.9: Tranverse Momentum of charge leptons of ZZ and $t\bar{t}$ background.

5.9 (right) represents the p_T of charge leptons.

P_T of Signal and Background

In Figure 5.10, we have plotted p_T of background on a signal. The transverse momentum of a signal corresponds to $\sin\theta = 0.7$. The rest of the parameters are set to (2.6.3) using $M_a = 400 \text{ GeV}$ $M_A = M_H = M_H^\pm = 700 \text{ GeV}$. In the Figure, we observed that if we apply cut on a $P_T \geq 150 \text{ GeV}$, the background will be discriminated.

5.6 Pseudorapidity of Signal and Background

The pseudorapidity of a particle is defined as the angle between the particle's motion direction and the beam's axis. Pseudorapidity is often used in collider experiments, such

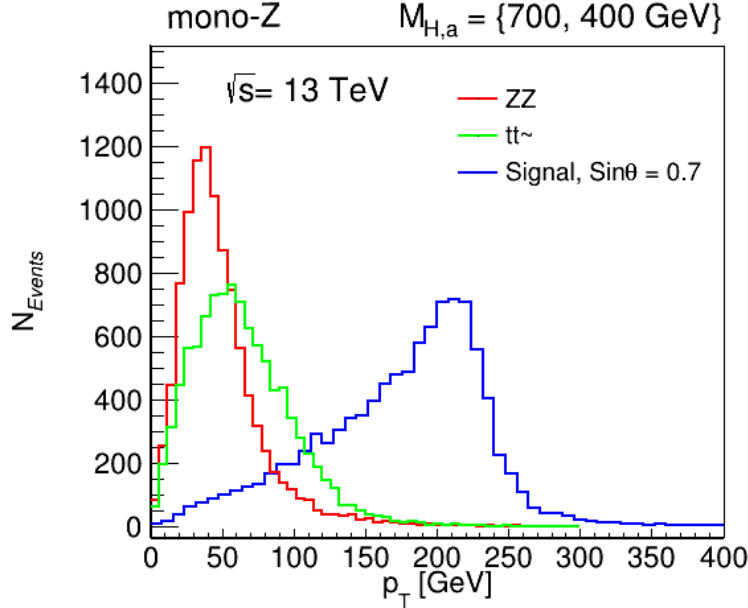


Figure 5.10: Tranverse Momentum of signal and background.

as LHC, as a method for describing the kinematics of particles generated by collisions at high energies. Researchers can measure the angle of a particle's motion with respect to the beam axis without taking the particle's energy into consideration. This can be helpful in situations where the energy of the particle is not well-defined or is difficult to measure. Figure 5.11, represents the η distribution of signal, ZZ and $t\bar{t}$ backgrounds.

5.7 ϕ of Signal and Background

The azimuthal angle refers to the angle between the beam axis and the transverse momentum of a particle or jet of particles. Azimuthal angle is denoted by (ϕ). Figure 5.12 displays the signal, $t\bar{t}$ and ZZ background ϕ distributions.

5.8 delta Phi of $P_{T,Z}$ and P_T^{miss}

The difference in azimuthal angle between two particles or jets of particles is called delta phi ($\Delta\Phi$). It is often used to study correlations between particles produced in high energy collisions, like those that occur at LHC. A correlation is illustrated in Figure 5.13 among the transverse momentum of Z and missing transverse momentum. In the Figure, we can see that the $\Delta\phi = 3.1$. It means that the Z boson and $\chi\chi$ (Dark Matter

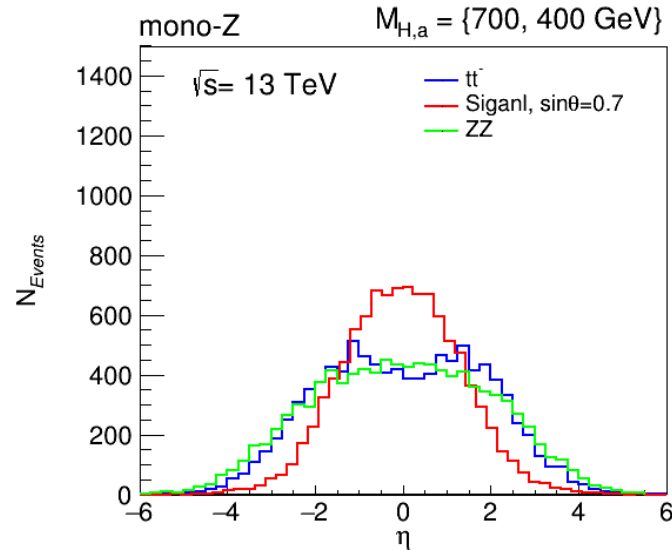


Figure 5.11: η distribution of signal and background.

Particles) are produced back to back.

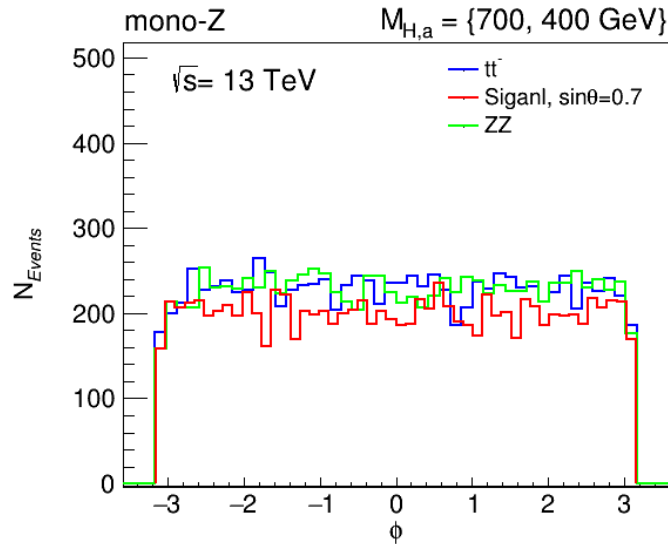


Figure 5.12: ϕ distribution of signal and background.

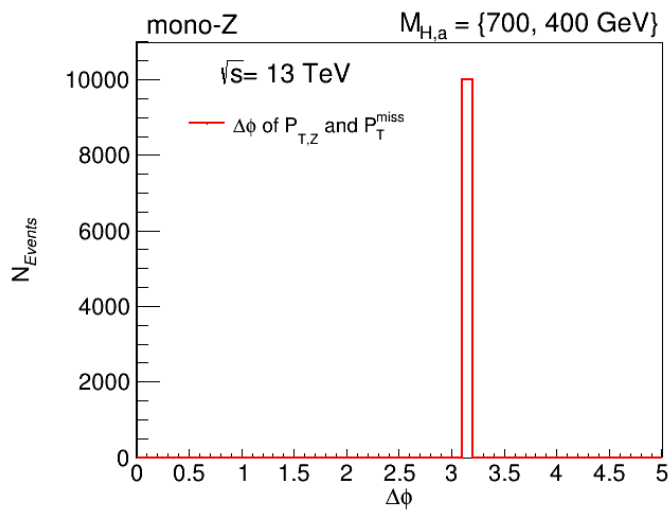


Figure 5.13: $\Delta\phi$ distribution of $P_{T,Z}$ and P_T^{miss} .

CHAPTER 6

The mono-Higgs($b\bar{b}$) + E_T^{miss} Analysis

The mono-h($b\bar{b}$) analysis was examined in this chapter and was carried out at $\sqrt{s}=13$ TeV using MadGraph5 aMC@NLO. Two Higgs Doublet Model + Pseduscalar (2HDM+a) is used for this analysis:

- 2HDM+a (discussed in detail in section 2.6.1) can produce several mono-X signatures. A signature where mediator 'a' is resonantly produced in association with the SM particle X. Then 'a' decays into a dark matter pair $\chi\chi$ producing a mono-X signal. In this chapter, will be only study h+ E_T^{miss}

By decaying heavy neutral Higg A to standard model 'h' boson a mediator 'a', where $a \rightarrow \chi\chi$, this model produces a mono-h signal. The specific signal studied in this analysis consists of two DM particles leaving the detector as missing transverse momentum with boosted 'h' boson decaying to ($b\bar{b}$).

The advantage of mono-H($b\bar{b}$) channel is that it allows for a more sensitive search for dark matter because it specifically targets the production of higgs bosons along with DM particles. This allows for a more targeted search and reduces background noise. The mono-H($b\bar{b}$) channel can be used in conjunction with other search channels to provide a more comprehensive understanding of dark matter. For example, it can be used to confirm or refute results obtained from other channels. There are strong theoretical motivations for mono-h($b\bar{b}$) channel, as it is predicted by many theories of dark matter. As a result, this channel is more likely to produce dark matter particles.

A disadvantage to using mono-H($b\bar{b}$) is that its sensitivity is limited to a certain range of dark matter masses. Due to the energy of the jet and missing transverse momentum, the sensitivity of this search depends on the energy of the collider. As a result, the mono-H($b\bar{b}$) channel may not be sensitive to dark matter particles that are too heavy or too light. Overall, the mono-H($b\bar{b}$) channel is a useful search strategy for dark matter.

6.1 Signal samples

The mono-H ($b\bar{b}$)+ E_T^{miss} signal samples have been studied using MadGraph with the Pseudoscalar_2HDM UFO model, The Parton Distribution Function (PDFs) used for analysis is NNPDF23_lo_as_0130 and PYTHIA 8.3 for parton showering. In MadGraph5, the gluon-gluon fusion process is generated using the following syntax:

```
MG5_aMC > import model Pseudoscalar_2HDM
MG5_aMC > generate g g > h1 xd xd~ [noborn=QCD]
```

Here xd and $xd\sim$ are dark matter particles and antiparticles have Particle Data Group IDs are 52 and -52 respectively. The noborn ensures that no tree-level contribution will be included and QCD ensures that only color charge particles (quarks and gluons) will participate in the loop.

The mono-H signal can also be produced by $b\bar{b}$ fusion. The MadGraph5 syntax used to generate the $b\bar{b}$ fusion process is .

```
MG5_aMC > import model Pseudoscalar_2HDM - bbMET_5FS
MG5_aMC > generate p p > h1 xd xd~
```

6.2 SM Background Processes

Backgrounds refer to all processes that result in the same final state as our signal. SM processes can result in a mono-h(bb) signature in addition to potential DM signals. Z+jets, $t\bar{t}$, and W+jets are the three main backgrounds estimated from MC simulation.

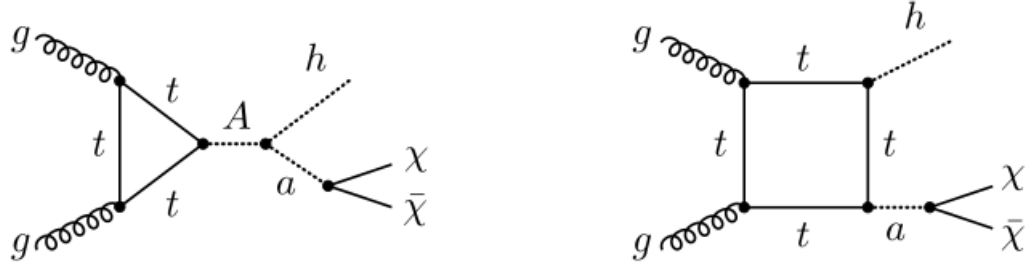


Figure 6.1: The Feynman diagrams show the 2HDM+ a model processes where a heavy pseudoscalar A decay to Higgs and pseudoscalar a.

$t\bar{t}$, $Z+jets$ and $W+jets$ processes are three dominant backgrounds. Figure 6.2 illustrate Feynman's diagram of three major background processes. In the $Z+jets$ events, Z boson decay to $\nu\nu$ contributes to the background. There is a small contribution from other decay channels of the Z boson. Leptonic W -boson decays contribute the most to $W+jet$ events. The semi-leptonic decay of $t\bar{t}$ contributes the most to the background as compared to another decay channel of $t\bar{t}$.

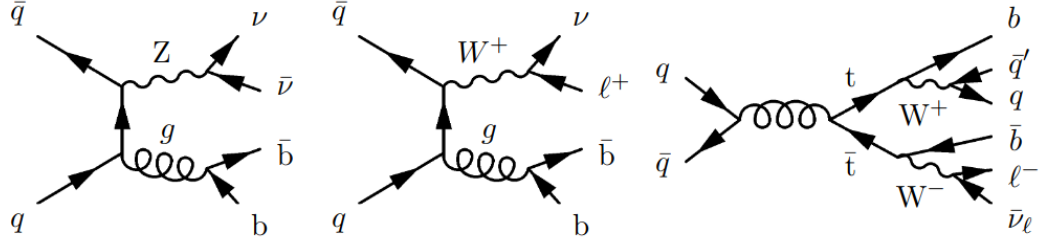


Figure 6.2: Feynman diagrams of $Z+jets$ (left), $W+jets$ (middle), and $t\bar{t}$ (right) background processes.

6.3 Variations of Parameter

To choose the best value for the analysis, we did scans for $\sin\theta$, $\tan\beta$ and m_χ .

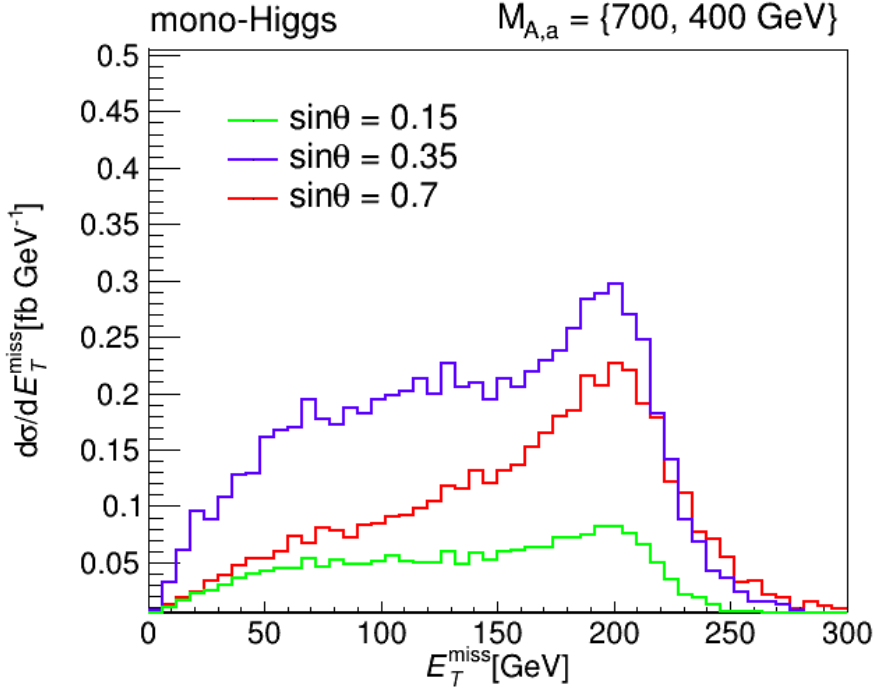


Figure 6.3: E_T^{miss} distributions for mono-higgs. The distribution corresponds to various values of $\sin\theta$. The rest of the parameters are set to (2.6.3) using $M_a = 400$ GeV and $M_A = M_H = M_H^\pm = 700$ GeV.

6.3.1 Variation of $\sin\theta$

In $h+E_T^{miss}$ analysis, The heavy neutral Higgs (A) decays to the "h" boson and the pseudoscalar 'a. where $a \rightarrow \chi\chi$. The mixing angle between the two neutral, CP-odd Higgs bosons is θ .

For various values of $\sin\theta$, Figure 6.3 displays E_T^{miss} distributions of $h + E_T^{miss}$ production. The remaining parameters are set to (2.6.3), with the spin-0 masses set to $M_a = 400$ GeV and $M_A = M_H = M_H^\pm = 700$ GeV. It has been shown that changing $\sin\theta$ leads in changes to the shape as well as the cross section.

From Figure 6.3 It is observed that at $\sin\theta= 0.35$ signal sensitivity enhanced.

6.3.2 Variation of $\tan\beta$

The ratio of the Vacuum Expectation Values (VEVs) of the two CP even Higgs bosons, h/H , is known as the $\tan\beta$. We choose different values of $\tan\beta$ and plot them against the

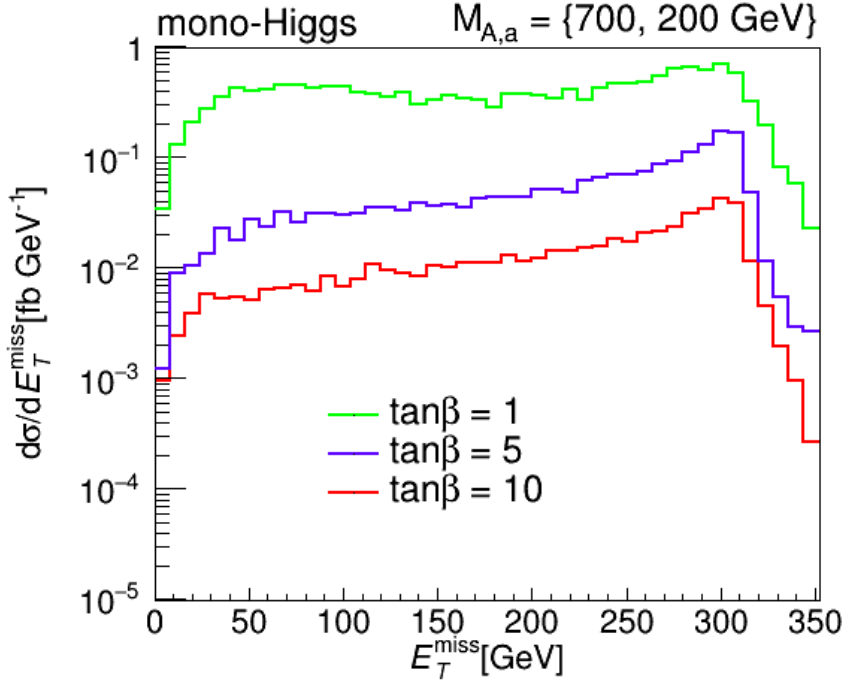


Figure 6.4: E_T^{miss} distributions for mono-Higgs production in gg-fusion in the 2HDM + a model. The predictions shown correspond to pp collisions at 13 TeV. The 2HDM + a parameters are set to (2.6.3) using $M_H = M_A = M_H^\pm = 700$ GeV and $M_a = 200$ GeV.

differential distributions. As we can see in the figure, as the value of $\tan\beta$ is increasing, the differential distributions is decreasing, that's why we chose $\tan\beta = 1$ in the benchmark parameters.

Figure 6.4 shows E_T^{miss} spectra for various $\tan\beta$ selections in the gg-fusion channel. It is observed that the total production cross section in gg fusion strongly decreases with increasing $\tan\beta$ for parameters $M_a = 200$ GeV and $M_A = M_H = M_H^\pm = 700$ GeV.

6.3.3 Variation of m_χ

The spectrum of $h + E_T^{miss}$ production under a variation of m_χ is shown in Fig. 6.5 (right). The given distributions are corresponding to benchmark parameters in (2.6.3) with $M_a = 300$ GeV and $M_A = M_H = M_H^\pm = 700$ GeV. The green and blue histograms correspond to the scenario with $M_a > 2m_\chi$ lead to almost identical rates of E_T^{miss} spectra. while the red histogram corresponds to the scenario where $M_a < 2m_\chi$ which is kinematically not allowed that's why the cross section is low and the shape is also

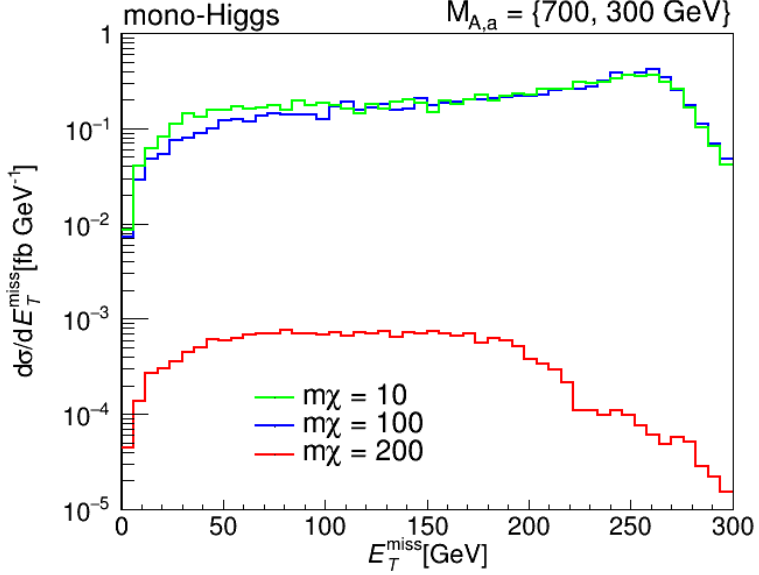


Figure 6.5: E_T^{miss} distributions for mono-h production. The distribution corresponds to different values of m_χ . Other parameters are set to (2.6.3) using $M_a = 300$ GeV and $M_A = M_H = M_H^\pm = 700$ GeV.

changed.

6.4 Variation of Energy

To study the effect of energies on the signal, we have produced the mono Higgs signal at 13, 13.6, 27, and 100 TeV. we have plotted the E_T^{miss} distribution vs the cross section. From Figure 6.6, it seems that the effect of varying energies is almost negligible at the generator level. There might be differences in the significance of the signal at different energies but the cross-section is almost the same as shown in Figure 6.6.

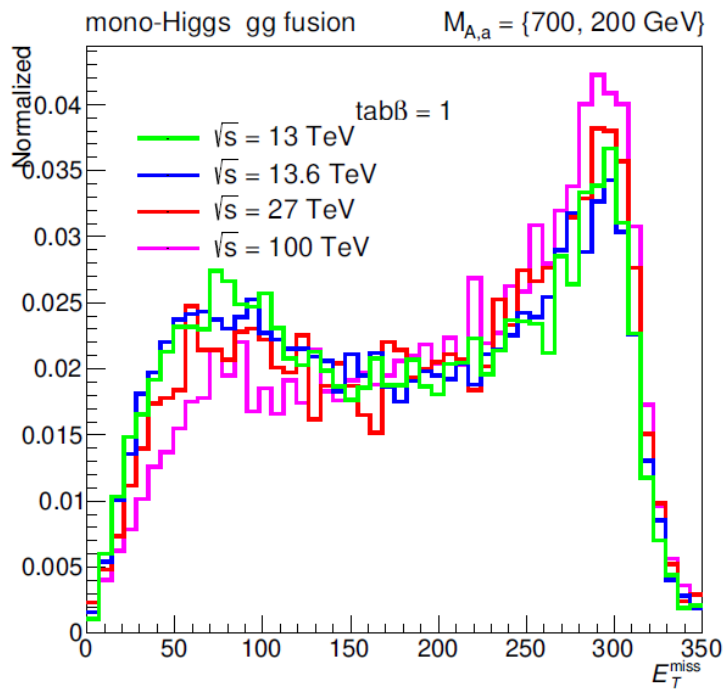


Figure 6.6: E_T^{miss} distributions for mono-h production at 13, 13.6, 27, and 100 TeV. The presented results correspond to $\tan\beta = 1$. Other parameters are set to (2.6.3) using $M_a = 200 \text{ GeV}$ and $M_A = M_H = M_H^\pm = 700 \text{ GeV}$.

CHAPTER 7

Summary and Conclusions

Cosmological observations indicate the existence of dark matter in our Universe. Those measurements do not provide information about the nature of Dark Matter. In spite of being regarded as a successful model, the Standard Model of particle physics doesn't provide information about Dark Matter candidates. To overcome this limitation, new physics models are needed beyond the Standard model. At colliders such as LHC, dark matter can be produced if it interacts with Standard model particles. In this way, we can study dark matter interactions in depth. By discovering the Higgs boson, the search for dark matter at LHC opened up a new field for research: DM particles with mass can interact with the Higgs through weak force.

This thesis presents an analysis of Dark Matter particles produced in an association of Higgs and Z bosons. Based on simulated proton-proton collision data generated by *MadGraph5_aMC@NLO* at $\sqrt{s} = 13$ TeV, the search is conducted. This search considers the Higgs decay to a pair of bottom quarks plus a substantial amount of missing transverse energy as the Higgs decay channel. This search is called the “mono-Higgs” search. Despite being only sensitive to a limited range of dark matter masses, mono-H(bb) allows for a more targeted search, as well as reducing background noise. In order to understand the dark matter more comprehensively, mono-h(bb) can be used in conjunction with other search channels. As part of the analysis strategy, a signal region should be defined where dark matter is enhanced over standard model backgrounds. In order to select signal regions, we exploit the kinematic differences between the dark matter and the background processes. A benchmark model (Two Higgs doublet model with light pseudoscalar, "2HDM+a") has been used for interpreting the results. The

Higgs \rightarrow bb decay channel has been examined with this model. As a result of proton proton collisions by gluon gluon fusion, a heavy pseudoscalar A is produced, which decays to the SM Higgs boson and to a light pseudoscalar a, which decays into the pair of DM particles χ . At the generator level, there is no significant difference in the cross section of mono-Higgs signals produced at 13, 13.6, 27, and 100 TeV.

During the search, we considered the Z boson decay to two oppositely charged leptons plus a considerable amount of missing transverse energy. This search is called the “mono-Z” search. Although the mono-Z($\ell\ell$) channel has a very small cross-section in comparison to the mono-jet, the advantage is that charged leptons are relatively easy to reconstruct in detectors as compared to jets. Furthermore, the large multijet background can be removed using a jet veto. In this analysis method, a signal region is defined where the dark matter signal is enhanced over the standard model background. Two Higgs doublet model extended by light pseudoscalar (described as "2HDM+a") has been used as a benchmark model to interpret the results. We examined this model in the decay channel $Z \rightarrow \ell+\ell-$. According to this model, a heavy neutral Higgs H decays into a Z boson and a pseudoscalar 'a', which decays into a pair of dark matter particles ($a \rightarrow \chi\chi$). Based on the results, we have concluded that the signal significance is high at $E_T^{miss} = 150$ GeV, while $p_T \geq 150$ GeV strongly discriminates the background rate.

Multivariate analysis techniques, specifically boosted decision trees, are needed to increase the analysis' sensitivity.

Bibliography

- [1] David Griffiths. *Introduction to elementary particles*. John Wiley & Sons, 2020.
- [2] Niels Walet. The basic building blocks for qcd feynman diagrams, 2010. URL <https://oer.physics.manchester.ac.uk/NP/Notes/Notesesse54.xht>.
- [3] Alexander Belyaev and Douglas Ross. *Weak Interactions*, pages 267–282. Springer International Publishing, Cham, 2021.
- [4] Corrinne Mills. Higgs’s production mode cross section, 2015. URL <https://slideplayer.com/slide/6970308/>.
- [5] Toni Šćulac. *Measurements of Higgs boson properties in the four-lepton channel in pp collisions at centre-of-mass energy of 13 TeV with the CMS detector*. PhD thesis, University of Zagreb. Faculty of Science. Department of Physics, 2018.
- [6] Erica Hupp, Steve Roy, and Megan Watzke. Nasa finds direct proof of dark matter. *Press Release*, 2006.
- [7] Stefano Giagu. Wimp dark matter searches with the atlas detector at the lhc. *Frontiers in Physics*, 7:75, 2019.
- [8] Tomohiro Abe, Yoav Afik, Andreas Albert, Christopher R Anelli, Liron Barak, Martin Bauer, J Katharina Behr, Nicole F Bell, Antonio Boveia, Oleg Brandt, et al. Physics of the dark universe. 2019.
- [9] Y Nie, R Schmidt, V Chetvertkova, G Rosell-Tarragó, F Burkart, and D Wollmann. Numerical simulations of energy deposition caused by 50 mev—50 tev proton beams in copper and graphite targets. *Physical Review Accelerators and Beams*, 20(8):081001, 2017.
- [10] Andrea Bastianin and Massimo Florio. Social cost-benefit analysis of hl-lhc. 2018.

- [11] CMS Collaboration, S Chatrchyan, G Hmayakyan, V Khachatryan, AM Sirunyan, W Adam, T Bauer, T Bergauer, H Bergauer, M Dragicevic, et al. The cms experiment at the cern lhc. *JInst*, 3:S08004, 2008.
- [12] Olga Kodolova, Michael Murray, Cms Collaboration, et al. Heavy ion physics with cms. *Nuclear Physics A*, 830(1-4):97c–104c, 2009.
- [13] Steven Maria A Mortier. *Exploring top-quark and Z boson coupling in top pair production in association with a Z boson*. PhD thesis, Gent U., 2020.
- [14] Lorenzo Viliani, CMS Collaboration, et al. Cms tracker performance and readiness for lhc run ii. *Nuclear Instruments and Methods in Physics Research Section A: Accelerators, Spectrometers, Detectors and Associated Equipment*, 824:67–69, 2016.
- [15] N Parashar. Cms pixel detector upgrade. *arXiv preprint arXiv:1110.2125*, 2011.
- [16] Rudolf Frühwirth and Are Strandlie. *Pattern Recognition, Tracking and Vertex Reconstruction in Particle Detectors*. Verlag der Österreichischen Akademie der Wissenschaften, 2021.
- [17] Reham Aly. *Search for Dark Matter Produced in Association With a Higgs Boson in the Four Leptons Final State Using Run II Data at $\sqrt{s} = 13$ TeV With the CMS Experiment*. PhD thesis, Bari U., 2021.
- [18] Calibration of the cms hadron calorimeters using proton-proton collision data at $\sqrt{s} = 13$ tev author=CMS collaboration and others, journal=arXiv preprint arXiv:1910.00079, year=2019.
- [19] Ettore Focardi. Status of the cms detector. *Physics Procedia*, 37:119–127, 2012.
- [20] CMS Collaboration. The phase-2 upgrade of the cms tracker. *CERN, Geneva, Tech. Rep. CERN-LHCC-2017-009. CMS-TDR-014*, 2017.
- [21] W Adam, Thomas Bergauer, D Bloech, E Brondolin, Marko Dragicevic, R Frühwirth, V Hinger, H Steininger, W Beaumont, D Di Croce, et al. Beam test performance of prototype silicon detectors for the outer tracker for the phase-2 upgrade of cms. *Journal of Instrumentation*, 15(03):P03014, 2020.
- [22] D Barney, CMS Collaboration, et al. Overview slide of ce with main parameters, 2019.

- [23] Stefan Höche. Introduction to parton-shower event generators. In *Journeys Through the Precision Frontier: Amplitudes for Colliders: TASI 2014 Proceedings of the 2014 Theoretical Advanced Study Institute in Elementary Particle Physics*, pages 235–295. World Scientific, 2016.
- [24] Keith A Olive, Kaustubh Agashe, Claude Amsler, Mario Antonelli, Jean-Francois Arguin, David M Asner, H Baer, Henry R Band, RM Barnett, Tullio Basaglia, et al. Review of particle physics. *Chinese physics C*, 38(9):090001, 2014.
- [25] Nathal Severijns. Weak interaction studies by precision experiments in nuclear beta decay. In *The Euroschool Lectures on Physics with Exotic Beams, Vol. I*, pages 339–381. Springer, 2004.
- [26] Yu M Antipov, VA Batarin, VA Bessubov, NP Budanov, Yu P Gorin, SP Denisov, IV Kotov, AA Lebedev, AI Petrukhin, SA Polovnikov, et al. Measurement of π -meson polarizability in pion compton effect. *Physics Letters B*, 121(6):445–448, 1983.
- [27] Ernest Rutherford. Lxxix. the scattering of α and β particles by matter and the structure of the atom. *The London, Edinburgh, and Dublin Philosophical Magazine and Journal of Science*, 21(125):669–688, 1911.
- [28] James Chadwick. The existence of a neutron. *Proceedings of the Royal Society of London. Series A, Containing Papers of a Mathematical and Physical Character*, 136(830):692–708, 1932.
- [29] Tsung-Dao Lee and Chen-Ning Yang. Question of parity conservation in weak interactions. *Physical Review*, 104(1):254, 1956.
- [30] Sheldon L Glashow. Partial-symmetries of weak interactions. *Nuclear physics*, 22(4):579–588, 1961.
- [31] Martin L Perl. The discovery of the tau lepton. Technical report, Stanford Linear Accelerator Center, 1992.
- [32] Po Bagnaia, M Banner, R Battiston, Ph Bloch, F Bonaudi, K Borer, M Borghini, J-C Chollet, AG Clark, C Conta, et al. Evidence for $z0 \rightarrow e^+ e^-$ at the cern pp collider. *Physics Letters B*, 129(1-2):130–140, 1983.

- [33] Marcela Carena, Sven Heinemeyer, Oscar Stål, CEM Wagner, and Georg Weiglein. Mssm higgs boson searches at the lhc: benchmark scenarios after the discovery of a higgs-like particle. *The European Physical Journal C*, 73(9):1–20, 2013.
- [34] Nabila Aghanim, Yashar Akrami, Frederico Arroja, Mark Ashdown, J Aumont, Carlo Baccigalupi, M Ballardini, Anthony J Banday, RB Barreiro, Nicola Bartolo, et al. Planck 2018 results-i. overview and the cosmological legacy of planck. *Astronomy & Astrophysics*, 641:A1, 2020.
- [35] Robert R Caldwell. A phantom menace? cosmological consequences of a dark energy component with super-negative equation of state. *Physics Letters B*, 545(1-2):23–29, 2002.
- [36] Thomas Adam, N Agafonova, A Aleksandrov, O Altinok, P Alvarez Sanchez, A Anokhina, S Aoki, A Ariga, T Ariga, D Autiero, et al. Measurement of the neutrino velocity with the opera detector in the cngs beam. *Journal of High Energy Physics*, 2012(10):1–37, 2012.
- [37] MP Decowski, KamLAND Collaboration, et al. Kamland’s precision neutrino oscillation measurements. *Nuclear Physics B*, 908:52–61, 2016.
- [38] K Abe, J Adam, H Aihara, T Akiri, C Andreopoulos, S Aoki, Akitaka Ariga, Tomoko Ariga, S Assylbekov, D Autiero, et al. Observation of electron neutrino appearance in a muon neutrino beam. *Physical review letters*, 112(6):061802, 2014.
- [39] Fritz Zwicky. Die rotverschiebung von extragalaktischen nebeln. *Helvetica physica acta*, 6:110–127, 1933.
- [40] VC Rubin and WK Ford Jr. Rotation of the andromeda nebula from a spectroscopic survey of emission regions <https://doi.org/10.1086/150317> astrophys, 1970.
- [41] E Pécontal, T Buchert, Ph Di Stefano, Y Copin, and K Freese. Review of observational evidence for dark matter in the universe and in upcoming searches for dark stars. *European Astronomical Society Publications Series*, 36:113–126, 2009.
- [42] M Bartelmann and P Schneider. Weak gravitational lensing [https://doi.org/10.1016/s0370-1573\(00\)00082-x](https://doi.org/10.1016/s0370-1573(00)00082-x) phys, 2001.

- [43] Nicolò Trevisani. Collider searches for dark matter (atlas+ cms). *Universe*, 4(11):131, 2018.
- [44] J Abdallah, H Araujo, A Arbey, A Ashkenazi, A Belyaev, et al. Simplified models for dark matter searches at the lhc, *phys. dark univ.* 9-10 (2015) 8–23. *arXiv preprint arXiv:1506.03116*, 2.
- [45] Jalal Abdallah, Henrique Araujo, Alexandre Arbey, Adi Ashkenazi, Alexander Belyaev, Joshua Berger, Celine Boehm, Antonio Boveia, Amelia Brennan, Jim Brooke, et al. Simplified models for dark matter searches at the lhc. *Physics of the Dark Universe*, 9:8–23, 2015.
- [46] John F Gunion and Howard E Haber. Cp-conserving two-higgs-doublet model: the approach to the decoupling limit. *Physical Review D*, 67(7):075019, 2003.
- [47] Martin Bauer, Ulrich Haisch, and Felix Kahlhoefer. Simplified dark matter models with two higgs doublets: I. pseudoscalar mediators. *Journal of High Energy Physics*, 2017(5):1–38, 2017.
- [48] Giorgio Arcadi, Giorgio Busoni, Thomas Hugle, and Valentin Titus Tenorth. Comparing 2hdm+ scalar and pseudoscalar simplified models at lhc. *Journal of High Energy Physics*, 2020(6):1–37, 2020.
- [49] Tomohiro Abe, Yoav Afik, Andreas Albert, Christopher R Anelli, Liron Barak, Martin Bauer, J Katharina Behr, Nicole F Bell, Antonio Boveia, Oleg Brandt, et al. Lhc dark matter working group: Next-generation spin-0 dark matter models. *Physics of the Dark Universe*, 27:100351, 2020.
- [50] G Arnison, A Astbury, B Aubert, C Bacci, G Bauer, A Bezaguet, R Böck, TJV Bowcock, M Calvetti, P Catz, et al. Experimental observation of lepton pairs of invariant mass around 95 gev/c² at the cern sps collider. *Physics Letters B*, 126(5):398–410, 1983.
- [51] V Fanti et al. Na48 collaboration. *Nucl. Instrum. Methods A*, 574:433, 2007.
- [52] Jonathan Hollar, Aruna Nayak, Betty Calpas, Nuno Almeida, Pedrame Bargassa, Andre David Tinoco Mendes, Pietro Faccioli, Pedro Guilherme Ferreira Parracho, Michele Gallinaro, Pedro Quinaz Ribeiro, et al. Observation of a new boson at a mass of 125 gev with the cms experiment at the lhc. 2012.

- [53] Lyndon Evans and Philip Bryant. Lhc machine. *Journal of instrumentation*, 3(08):S08001, 2008.
- [54] LHC Guide. Mar 2017. URL <https://cds.cern.ch/record/2255762>.
- [55] ATLAS collaboration et al. Physics at a high-luminosity lhc with atlas. *arXiv preprint arXiv:1307.7292*, 2013.
- [56] CMS collaboration et al. Description and performance of track and primary-vertex reconstruction with the cms tracker. *Journal of Instrumentation*, 9(10):P10009, 2014.
- [57] Nathaniel Woods. *ZZ Production in Proton-Proton Collisions at $s = 13 \text{ TeV}$ in Four-Lepton Events Using the CMS Detector at the LHC*. The University of Wisconsin-Madison, 2017.
- [58] Nicolas Maximilian Rowert. *Assembly and Characterization of a First Functional 2S Module for the CMS Phase-2 Upgrade at LHC*. PhD thesis, Rheinisch Westfaelische Tech. Hoch.(DE), 2017.
- [59] F Arteche and C Rivetta. Emc diagnosis and corrective actions for silicon strip tracker detectors. Technical report, SLAC National Accelerator Lab., Menlo Park, CA (United States), 2006.
- [60] Michael Pöttgens. Development and evaluation of test stations for the quality assurance of the silicon micro-strip detector modules for the cms experiment. 2007.
- [61] Laura Borrello, Ettore Focardi, Anna Macchiolo, and Alberto Messineo. Sensor design for the cms silicon strip tracker. Technical report, CERN-CMS-NOTE-2003-020, 2003.
- [62] CMS collaboration et al. The phase-2 upgrade of the cms tracker. *CMS-TDR-014*, 2017.
- [63] Michael H Seymour and Marilyn Marx. Monte carlo event generators. *LHC Phenomenology*, pages 287–319, 2015.
- [64] G Marchesini and Bryan R Webber. Simulation of qcd jets including soft gluon interference. *Nuclear Physics B*, 238(1):1–29, 1984.

- [65] Torbjörn Sjöstrand. Status of fragmentation models. *International Journal of Modern Physics A*, 3(04):751–823, 1988.
- [66] Torbjörn Sjöstrand. The pythia event generator: past, present and future. *Computer Physics Communications*, 246:106910, 2020.
- [67] Johan Alwall, Michel Herquet, Fabio Maltoni, Olivier Mattelaer, and Tim Stelzer. Madgraph 5: going beyond. *Journal of High Energy Physics*, 2011(6):1–40, 2011.
- [68] Carlo Oleari. The powheg-box. *arXiv preprint arXiv:1007.3893*, 2010.
- [69] Baradhwaj Coleppa, Felix Kling, and Shufang Su. Constraining type ii 2hdm in light of lhc higgs searches. *Journal of High Energy Physics*, 2014(1):1–32, 2014.
- [70] Richard D Ball, Valerio Bertone, Stefano Carrazza, Christopher S Deans, Luigi Del Debbio, Stefano Forte, Alberto Guffanti, Nathan P Hartland, José I Latorre, Juan Rojo, et al. Parton distributions for the lhc run ii. *Journal of High Energy Physics*, 2015(4):1–148, 2015.
- [71] Richard D Ball, Valerio Bertone, Stefano Carrazza, Christopher S Deans, Luigi Del Debbio, Stefano Forte, Alberto Guffanti, Nathan P Hartland, José I Latorre, Juan Rojo, et al. Parton distributions with lhc data. *Nuclear Physics B*, 867(2):244–289, 2013.
- [72] Ilka Antcheva, Maarten Ballintijn, Bertrand Bellenot, Marek Biskup, Rene Brun, Nenad Buncic, Ph Canal, Diego Casadei, Olivier Couet, Valery Fine, et al. Root—a c++ framework for petabyte data storage, statistical analysis and visualization. *Computer Physics Communications*, 180(12):2499–2512, 2009.